

Observation of Perfect Absorption in Hyperfine Levels of Molecular Spins with Hermitian Subspaces

Claudio Bonizzoni^{1,2*}, Daniele Lamberto³, Samuel Napoli³, Simon Günzler⁴, Dennis Rieger⁴, Fabio Santanni⁵, Alberto Ghirri², Wolfgang Wernsdorfer⁴, Salvatore Savasta³, Marco Affronte^{1,2}

^{1*}Dipartimento di Scienze Fisiche, Informatiche e Matematiche, Università di Modena e Reggio Emilia, via G. Campi 213/a, Modena, 41125, Italy.

²Istituto Nanoscienze, CNR, via G. Campi 213/a, Modena, 41125, Italy.

³Dipartimento di Scienze matematiche e informatiche, scienze fisiche e scienze della terra, Università degli Studi di Messina, Via Salita Sperone, c.da Papardo, Messina, 98166, Italy.

⁴Physikalisches Institut, Karlsruhe Institute of Technology, Wolfgang-Gaede-Str. 1, Karlsruhe, D-76131, Germany.

⁵Dipartimento di Chimica Ugo Schiff, Università degli Studi di Firenze, via della Lastruccia 3, Sesto Fiorentino (FI), 50019, Italy.

*Corresponding author(s). E-mail(s): claudio.bonizzoni@unimore.it;

Abstract

Ideal effective parity-time (PT)-symmetry can be achieved in a passive open system by accurately balancing feeding and absorption processes. Such PT-symmetric systems display Hermitian subspaces which enable *perfect absorption* (PA) of radiation, *i.e.*, all the incoming energy is absorbed by the system. In this work, we consider a passive open quantum system obtained by coupling molecular spin centers to a planar microwave resonator operating at milliKelvin temperatures and at few-photon power level. We experimentally demonstrate that Hermitian subspaces and thus PA can be implemented even in the absence of PT-symmetry, by exploiting the spin detuning to control the photon and spin content of a polariton mode. In such a way, the required balance between the feeding and the loss rates is effectively recovered. We show that Hermitian subspaces

influence the overall aspect of coherent spectra of cavity QED systems and significantly enlarge the possibility to explore non-Hermitian effects in open quantum systems. We finally discuss how Hermitian subspaces can be potentially exploited for the development of efficient switches and modulators with high modulation depths over a broad spectral range.

Keywords: perfect absorption, open quantum systems, molecular spins, microwaves, hermiticity

Open systems with parity-time (PT)-symmetry have attracted a great deal of interest in the last decades following the pioneering works of Bender and Boettcher [1, 2], who showed that systems described by non-Hermitian Hamiltonians and displaying PT-symmetry can have entirely real-valued energy spectra. These ideal PT systems exhibit a balanced absorption (loss) and amplification (gain) [3, 4]. Yet, the requirement of balanced gain and losses is difficult to achieve in practice, limiting their experimental observations and possible applications. It has been shown that an ideal effective PT-symmetry can also be implemented using only passive open quantum systems, regarding the feeding field as an effective gain [5, 6]. Here, the input-output rate through the feeding port/s balances the losses associated to each component of the system, leading to a *critical coupling* condition and to *perfect absorption* (PA). This occurs in the presence of real eigenfrequencies of the effective non-Hermitian Hamiltonian describing the system and it is observed when the driving frequency matches such values. Absorption, which is typically regarded as an undesired effect, can actually improve the performance of operations, such as detection, quantum state transfer and wavelength conversion. Furthermore, PA and related phenomena may offer new opportunities in the development of optical modulators and switches.

PA has been observed in optics using microdisks [7], slab waveguides [8], optical metamaterials [9, 10], slabs of conductive materials [11] or nanostructured semiconductors [12]. These systems are constituted by passive components and are fed with one or more input signals. The necessary balance between incoming energy and losses is achieved by adjusting the coupling of the system with its feeding lines and/or the losses of the system. Similarly, PA can be realized at microwave frequencies using metamaterials [13], conducting films [14, 15], microwave resonators [5, 6] or dielectrics [16]. Similar results have been obtained using microwave cavities coupled to ferromagnetic Yttrium-Iron-Garnet (YIG) spheres [17–19]. Here, the system typically has a two ports configuration, which are used to send microwave excitations and, due to the low damping of YIG, its magnetic coupling with the cavity is adjusted to obtain the necessary critical coupling condition.

Conversely, diluted spin centers in a non magnetic matrix offer the possibility to play with multiple degrees of freedom, for instance, by choosing the crystal field or the hyperfine interaction. These features can be tailored at synthetic level in molecular spin systems [20–23], along with their coherence times and further genuine quantum features [24–26]. These have been exploited for applications in quantum information

processing [27–30] and in quantum sensing [31–33]. Molecular spins can be embedded into hybrid spin-superconducting circuits [34–38] thus offering an ideal testbed to investigate open systems at microwave frequencies described by non-Hermitian Hamiltonians.

In this work, we investigate an open passive system which is not PT-symmetric, explicitly linking the presence of PA with the concept of Hermitian subspaces. Our geometry consists in a planar superconducting microwave resonator in the purely quantum regime (mK temperature and average single microwave photon number) overcoupled to its input-output line and magnetically coupled to molecular spin centers as depicted in Fig. 1. We first consider a diluted α, γ -bisdiphenylene- β -phenylallyl (BDPA, for short) organic radical spin as a prototypical Two-Level-System (TLS) and, then, an tetraphenylporphyrinato oxovanadium(IV) complex (VOTPP, for short), with large ($I = 7/2$) nuclear spin and anisotropic hyperfine tensor to enlarge the number of subsystem investigated (Fig. 1 (d)). Tuning the position of the sample on the resonator allows us to change the coupling rate with the spins, g_μ , thus crossing from the weak to the strong coupling regime. Moreover, the resulting non-equal thermal population of the hyperfine multiplet of VOTPP allows to map the effect of slightly different couplings by simply tuning the applied static magnetic field. We experimentally demonstrate that it is possible to obtain PA with zero reflection dips at energies values detuned from resonance, at two symmetric positions with respect to resonance. While this phenomenon had been previously investigated theoretically, albeit without any connection to non-Hermitian physics [39], our results provide a direct experimental confirmation consistent with theoretical predictions. Our theoretical analysis reveals that this corresponds to tailor effective Hermitian subspaces in our open quantum system, even when radiative and non-radiative losses are not balanced, thus in the absence of PT symmetry. The presence of these Hermitian subspaces largely shapes the overall aspect of the coherent spectra of light-matter systems as a function of detuning.

1 Theoretical modeling

We begin by presenting the model developed for our system, which is sketched in Fig. 1 (a,b) (see Methods for details). The resonator has frequency ω_0 , intrinsic (non-radiative) losses, γ_{nr} , and it is coupled to an antenna acting as an input-output port with rate γ_r . The μ -th spin ensemble is coupled to the resonator through its collective coupling strength g_μ , and has energy $\omega_{s\mu} = g_{L\mu}\mu_B B_0/\hbar$ (being B_0 the applied static magnetic field, g_L is an effective Landé g-factor and μ_B is the Bohr’s magneton) and intrinsic relaxation rate $\gamma_{s\mu}$. While BDPA can be effectively described using a single resonance frequency ($\mu = 1$), the VOTPP sample comprises multiple molecular spin levels due to hyperfine splitting ($\mu = 1, \dots, 8$), in Fig. 1 (d). These multiple-spin ensembles can be effectively described using the Holstein-Primakoff mapping with N non-interacting bosons. In the low-excitation regime, such mapping can be linearized, leading to the harmonic Hamiltonian

$$\hat{H}_S = \hbar\omega_0 \hat{a}^\dagger \hat{a} + \hbar \sum_{\mu=1}^N \omega_{s\mu} \hat{b}_\mu^\dagger \hat{b}_\mu + \hbar \sum_{\mu=1}^N g_\mu (\hat{a}^\dagger \hat{b}_\mu + \hat{b}_\mu^\dagger \hat{a}), \quad (1)$$

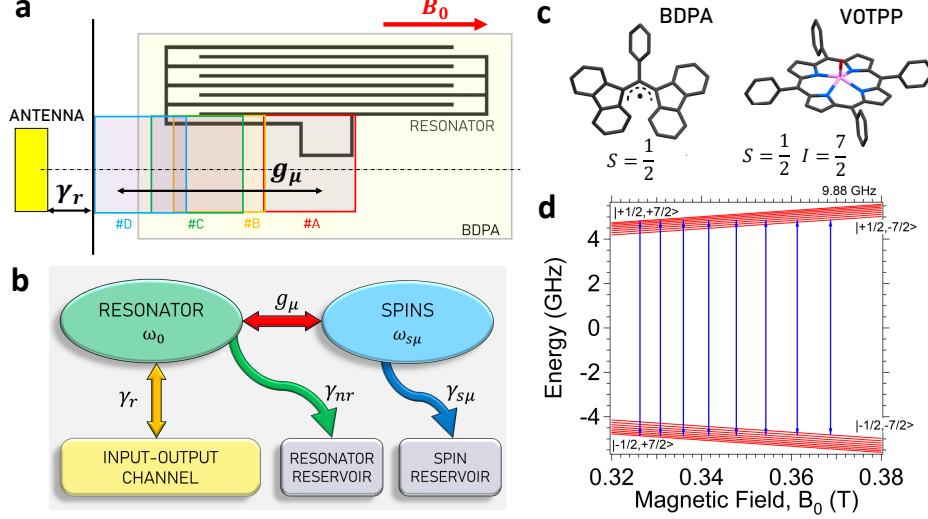


Figure 1 Implementing and modeling the open passive quantum system. **a** Sketch of the lumped element resonator with all sample positions investigated in this work. The large light-yellow rectangle represents the BDPA sample, while the smaller rectangles represent the different positions of the VOTPP crystal (#A to #D, from red to light-blue). The distance between the antenna (yellow) and the chip can be adjusted at room temperature to vary the radiative relaxation rate of the resonator γ_r . The position of the sample controls the coupling strength g_μ with the resonator. Red arrow shows the direction of the applied static magnetic field, B_0 . **b** Model adopted in this work for the open quantum system in **a**. The resonator is coupled to both spins and its input/output line (antenna). Only a single spin μ -th ensemble is shown for clarity. **c** Molecular structure for BDPA and VOTPP. Labels indicate their electronic $S = 1/2$ and nuclear $I = 7/2$ nuclear spins. Images reproduced from [20, 40] with permission. **d** Easyspin simulation of the $\{S_z, I_z\}$ energy levels of VOTPP obtained with the parameters and the Hamiltonian reported in [20, 36] at 9.88 GHz. Blue arrows show the eight allowed $|-\frac{1}{2}, I_z\rangle \leftrightarrow |\frac{1}{2}, I_z\rangle$ transitions giving the μ -th (sub)ensembles.

where \hat{a} and \hat{b}_μ denote the bosonic annihilation operators of the resonator and the μ -th spin ensemble. The coupling strengths g_μ observed are sufficiently small with respect to ω_0 to justify the use of the rotating wave approximation (RWA) [41]. Eq. (1) can describe either the BDPA system for $N = 1$ or the VOTPP sample for $N = 8$. The coupling with the external environment, which consists in the decay channels of the resonator (radiative and non-radiative) and of the spin ensembles (Fig. 1 (b)), can be conveniently described by Heisenberg-Langevin equations, which take into account also the coherent feeding field through the antenna (see Supplementary Material). The complex reflection scattering parameter, $S_{11}(\omega)$, can be shown to have poles corresponding to the complex eigenfrequencies, Ω_j , of the non-Hermitian Hamiltonian $\hat{H}_{\text{NH}}/\hbar = \hat{\alpha}^\dagger (\mathbf{A} - i\mathbf{\Gamma}/2) \hat{\alpha}$, where $\hat{\alpha}^T = (\hat{a}, \hat{\mathbf{b}})$, \mathbf{A} is the Hopfield matrix of Hamiltonian in Eq. (1) and $\mathbf{\Gamma}$ is the corresponding decay matrix. Moreover, we observe that the zeros of $S_{11}(\omega)$ exhibits the same structure as the denominator, with the only difference being the reversal of the sign of the decay rate associated with the input-output port, γ_r (see Methods) [39, 42]. These zeros are the complex eigenfrequencies, $\tilde{\Omega}_j$, of the

effective non-Hermitian Hamiltonian

$$\hat{H}_{\text{eff}}/\hbar = \hat{\boldsymbol{\alpha}}^\dagger (\mathbf{A} - i\tilde{\boldsymbol{\Gamma}}/2)\hat{\boldsymbol{\alpha}}, \quad (2)$$

where the decay matrix $\tilde{\boldsymbol{\Gamma}}$ differs from $\boldsymbol{\Gamma}$ only for the inversion of the sign of the input-output port decay rate (notice that $-\gamma_r$ corresponds to the feeding rate). Hence, the reflection scattering parameter reads

$$S_{11}(\omega) \propto \prod_{j=1}^{N+1} \frac{\omega - \tilde{\Omega}_j}{\omega - \Omega_j}. \quad (3)$$

Equation (3) explicitly highlights the connection between the PA condition ($S_{11}(\omega) = 0$) and the eigenvalues of the effective non-Hermitian Hamiltonian \hat{H}_{eff} in Eq. (2). Indeed, when the imaginary part of one of the complex eigenfrequencies of Eq. (2) vanishes ($\Im(\tilde{\Omega}_j) = 0$ for some j), it is always possible to nullify the numerator of S_{11} by appropriately tuning ω . To further elucidate this point, we first perform a rotation on the bare bosonic operators to transform them in the polariton basis (normal modes). Specifically, we introduce a suitable Hopfield transformation \mathbf{U} , defined as $\hat{\mathbf{P}} = \mathbf{U}\hat{\boldsymbol{\alpha}}$, such that the Hamiltonian of the isolated system in Eq. (1) takes the diagonal form $\hat{H}_S = \sum_{j=1}^{N+1} \bar{\omega}_j \hat{P}_j^\dagger \hat{P}_j$. Subsequently, the effective non-Hermitian Hamiltonian describing the open system dynamics is given by

$$\hat{H}_{\text{eff}} = \sum_{j=1}^{N+1} \left(\bar{\omega}_j - i\frac{\bar{\gamma}_j}{2} \right) \hat{P}_j^\dagger \hat{P}_j, \quad (4)$$

where the effective (or *dressed*) loss rates $\bar{\gamma}_j$ are defined by the diagonal elements of $\mathbf{U}\tilde{\boldsymbol{\Gamma}}\mathbf{U}^\dagger$ (see Supplementary Information). Here, we just remark that this Hamiltonian is derived under the hypothesis of perfect absorption and is valid in the strong coupling regime. In this regime, the mixed terms in the decay channels can be safely neglected due to the different resonance frequencies of the polaritonic peaks.

2 Results

2.1 The Single Ensemble Case

We first consider the BDPA sample, which allows us to test our model in the simple case of $N = 1$. Fig. 2 (a) displays reflection spectra maps as a function of the static magnetic field. An anticrossing, which is typical of the strong spin-photon coupling regime, is clearly visible when ω_s crosses ω_0 . We observe the presence of two dips (Fig. 2 (b)), approaching zero reflection, corresponding to PA. Remarkably, these occur before (0.3443 T) and after (0.3459 T) the resonant magnetic field value, corresponding to resonator-spin detuning $\Delta = \omega_0 - \omega_s \approx \pm 8 \cdot 10^{-4}$ T. This clearly differs from what is typically observed in PT-symmetric systems, where the dips occur at resonance [18]. We fit our data using Eq. (3), which accurately reproduces the observed anticrossing of the polaritonic modes and, most importantly, the positions and the absolute values

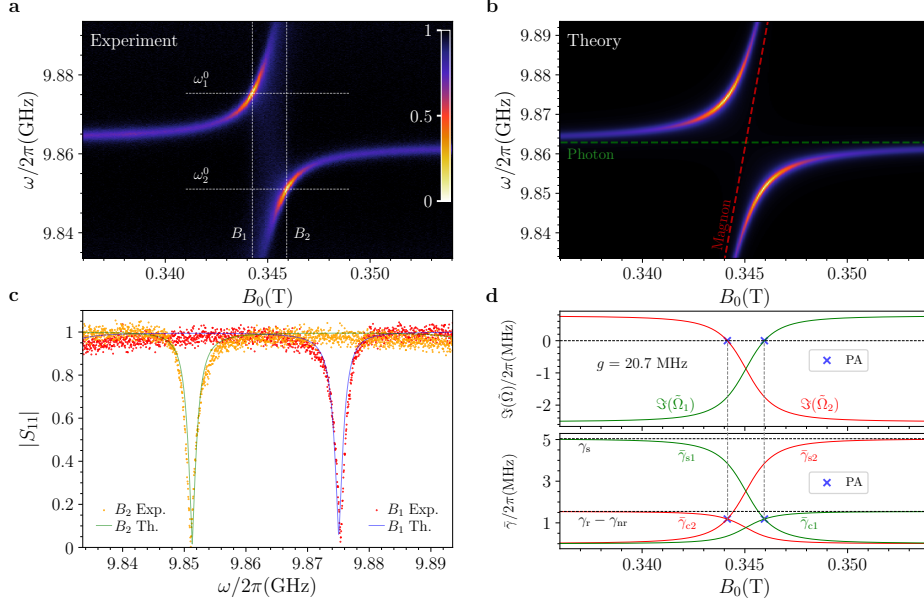


Figure 2 Perfect Absorption for the Single Ensemble Case. **a** Normalized reflection map ($|S_{11}(\omega)|$) measured for the BDPA sample at 25 mK as a function of the static magnetic field B_0 . **b** Simulated reflection map obtained using the fit parameters extracted from the map in panel **a**, according to Eq. (8) in Methods (fit parameters are reported in Table 1 of the Supplementary Information). **c** Theoretical (green and blue lines) and experimental (orange and red dots) normalized reflection spectra extracted from the maps in **a** and **b**, showing two dips with nearly zero reflection (see vertical lines B_1 and B_2 in panel **a**). **d** (Upper panel) Imaginary parts of $\tilde{\Omega}_{1,2}$, $[\Im(\tilde{\Omega}_{1,2})]$, as a function of B_0 , calculated using Eq. (3) and the fit parameters obtained from **a**. Perfect absorption (blue crosses) occurs at the polariton resonances when $\Im(\tilde{\Omega}_{1,2})$ crosses zero. **d** (Lower panel) Dressed cavity feeding rate $\tilde{\gamma}_{ci}$ and dressed spin loss rate $\tilde{\gamma}_{si}$ as functions of B_0 , computed according to Eq. (5). Perfect absorption (blue crosses) is achieved when $\tilde{\gamma}_{ci} = \tilde{\gamma}_{si}$ for the i -th polariton (see main text).

of the two reflection zeros (Fig. 2 (b)). As a first important result, we demonstrate (both experimentally and theoretically) that PA can be achieved even if the system does not display PT-symmetry. More specifically, in the strong coupling regime, the imaginary part of the j -th effective complex eigenfrequencies, $\Im(\tilde{\Omega}_j)$, is approximately equal to the effective loss rates $\tilde{\gamma}_j/2$ (as given by Eq. (4)), and it can be expressed by a linear combination of the single-channel loss rates (see Methods)

$$\tilde{\gamma}_j = (-\gamma_r + \gamma_{nr}) |U_{j1}|^2 + \gamma_s |U_{j2}|^2. \quad (5)$$

U_{jk} are the Hopfield coefficients defined by \mathbf{U} , which determines the degree of photon ($|U_{j1}|^2$) and spin ($|U_{j2}|^2$) hybridization of the polaritons, and which can be tuned through the spin-resonator detuning. Therefore, PA ($\tilde{\gamma}_j = 0$) occurs when the balance between dressed losses is achieved even in the absence of PT-symmetry. In our experiments this is realized by varying the detuning Δ through the magnetic field. Therefore, Eq. (5) can be satisfied for either the lower or upper polariton, leading to

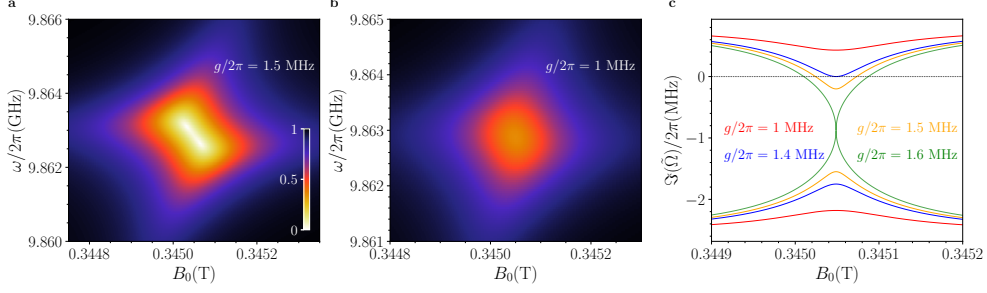


Figure 3 Perfect Absorption During the Transition from Strong to Weak Coupling Regime. **a, b** Normalized reflection ($|S_{11}|$) maps as a function of the static magnetic field B_0 , simulated using Eq. (8) in Methods with the parameters fitted from the data in Fig. 2, except for using lower coupling strength values of $g/2\pi = 1.5$ MHz (**a**) and $g/2\pi = 1$ MHz (**b**), respectively. **c** Imaginary parts of $\tilde{\Omega}_{1,2}$, $[\Im(\tilde{\Omega}_{1,2})]$, calculated as a function of the static magnetic field using the relaxation rates fitted from the data in Fig. 2 and four different values of $g/2\pi$. Perfect absorption occurs when $\Im(\tilde{\Omega}_{1,2})$ crosses zero and cannot be realized for $g/2\pi < 1.4$ MHz (see main text).

the emergence of a Hermitian subspace within the Hilbert space of \hat{H}_{eff} . This subspace $\mathcal{H}^{(j)}$ is effectively described by the Hamiltonian $\hat{H}_{\text{HS}}^{(j)} = \tilde{\omega}_j \hat{P}_j^\dagger \hat{P}_j$, where $j = 1$ or $j = 2$. Furthermore, it can be easily shown that if a Hermitian subspace exists for one of the polariton modes at a given detuning Δ' , a second one will exist at $-\Delta'$ for the other polariton mode. Fig. 2 (d) shows the imaginary part of the complex eigenvalues of Eq. (2), $\Im(\tilde{\Omega}_j)$, along with the corresponding contributions of the dressed cavity feeding rate, $\tilde{\gamma}_{cj} = (\gamma_r - \gamma_{\text{nr}}) |U_{j1}|^2$, and dressed spin loss rate, $\tilde{\gamma}_{sj} = \gamma_s |U_{j2}|^2$, to the j -th polariton mode. The balance between the two contributions ($\tilde{\gamma}_{cj} = \tilde{\gamma}_{sj}$) is observed for either of the polariton modes at symmetric detunings as also demonstrated by the simultaneous vanishing of $\Im(\tilde{\Omega}_j)$. This highlights also the connection of PA to non-Hermitian physics. As a final note, we evidence that this framework is consistent with the phenomenology previously observed in PT-symmetric systems, of which it can be regarded as a generalization. In particular, when $\gamma_r - \gamma_{\text{nr}} = \gamma_s$ (PT symmetry condition), the Hopfield coefficients must satisfy $|U_{j1}|^2 = |U_{j2}|^2 = 1/2$ in order to fulfill Eq. (5). This condition is met for $\Delta = 0$, indicating that PA occurs at resonance and simultaneously for both polariton modes.

We now investigate the effect of the coupling strength on PA. Fig. 3 shows reflection maps simulated with Eq. (8) by using the relaxation rates obtained from the fits of Fig. 2 along with different decreasing coupling strengths. Notably, as the coupling decreases the dips progressively merge towards the resonant field value. We identify a critical threshold, coinciding with the exceptional point condition $g_{\text{EP}} = (\gamma_r - \gamma_{\text{nr}} + \gamma_s)/4$ (green line in Fig. 3 (c)). An intermediate region emerges, where no crossing of the imaginary parts occurs but PA still persists (yellow line), until the coupling strength reaches a minimum value $g_{\text{min}} = \sqrt{(\gamma_r - \gamma_{\text{nr}})\gamma_s}/2$, at which $\Im(\tilde{\Omega}_j)$ exhibits a double root at zero detuning (blue line) and the reflection dips coalesce into a single one. For couplings below g_{min} the polaritonic loss rates cannot cross the zero, preventing the observation of PA (red line). It is worth mentioning that in

PT-symmetric systems $\Im(\tilde{\Omega}_i)$ is symmetric with respect to the real axis and gives a single zero at $\Delta = 0$. This also gives $g_{\text{EP}} = g_{\text{min}}$, and no intermediate region occurs as the coupling decreases. Hence, the presence of the crossing can be directly linked to the possibility of achieving PA.

2.2 The Multiple Ensemble Case

We now experimentally investigate the effect of the coupling strength by considering the eight resonances given by VOTPP. Overall, the coupling regime of the whole group of transitions mainly depends by the overlap between the microwave magnetic field of the resonator and the sample, hence by the position of the sample with respect to the resonator (see Fig. 1). In addition the values of the hyperfine tensor of VOTPP (see Methods) give different thermal population of hyperfine levels at 30 mK, thus allowing us to span a large set of g_j values within a unique field scan.

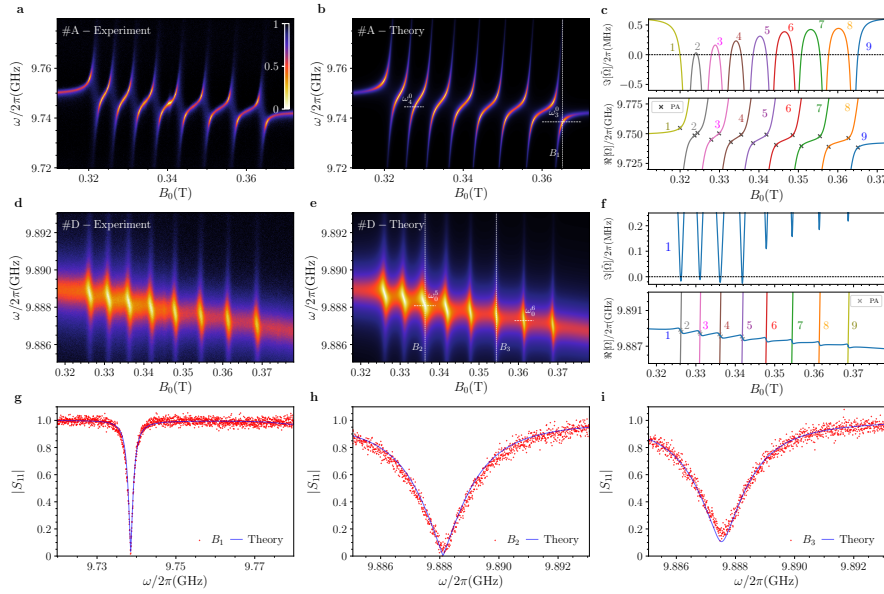


Figure 4 Perfect Absorption for the Multiple Spin Case. **a, d** Normalized reflection ($|S_{11}|$) maps measured as a function of the static magnetic field B_0 at 30 mK for the VOTPP crystal. PA is observed in proximity of multiple hyperfine levels. The strongest (position #A) and the weakest (position #D) coupling regimes are shown, respectively. **b, e** Simulated reflection maps obtained by fitting the maps in **a, d** according to Eq. (8) in Methods. **c, f** (Upper panels) Imaginary parts of the complex frequencies, $\Im(\tilde{\Omega}_j)$, as a function of the magnetic field B_0 , for the j -th polariton frequency. The horizontal black dotted line at $\Im(\tilde{\Omega}) = 0$ corresponds to the PA condition. **c, f** (Lower panels) Real parts of the polariton frequencies, $\Re(\Omega_j)$, with the predicted PA points, showing excellent agreement with the experimental data. Both $\Im(\tilde{\Omega}_j)$ and $\Re(\Omega_j)$ are calculated using Eq. (3) supported by Eq. (8) in Methods. **g, h, i** Experimental (red dots) and theoretical (blue lines) normalized reflection obtained according to the vertical lines shown in **b, e** (B_1 , B_2 , and B_3), displaying perfect absorption dips and one not satisfying this condition. All fit parameters are given in tables 5 and 8 of Supplementary Information.

Figure 4 (a, d) shows experimental reflection maps, $|S_{11}|$, measured as functions of the static magnetic field, for positions #A and #D of VOTPP (see Fig. 1). In position #A, the observed avoided level crossings clearly indicate that the high cooperativity regime is achieved on each line. A pair of dips in reflection, approaching near-zero values and at non-zero detuning from resonance, is clearly visible for each line, indicating the presence of PA. Conversely, data for position #D show significantly lower coupling strengths, denoting the weak coupling regime for all resonances. Here, only the first four spin ensembles display points of PA, and the coalescence of those dips is observed for increasing magnetic field values. The theoretical reflection maps in Fig. 4 (b,e), simulated through Eq. (3), are in excellent agreement with the data. For position #A the PA points can be perfectly predicted by the zeros of the imaginary parts of the corresponding effective eigenfrequencies (Fig. 4 (c)), calculated by using the fit parameters obtained from Fig. 4 (a). Conversely, for position #D the imaginary parts of the complex eigenvalues, $\Im(\tilde{\omega}_j)$, are zero only for the first four lines, while the remaining lines do not exhibit PA. This can be explained by the minimal coupling g_{\min} discussed in Sec. 2.1, since moving across the different resonances results in the coupling strengths g_j becoming smaller than g_{\min} . These latter results demonstrate that Eq. (3) holds also in the weak coupling regime, demonstrating that PA condition can be achieved provided that a minimum coupling rate value is overcome for a given set of relaxation rates.

3 Discussion

The observation of PA into a passive open quantum system without PT-symmetry, both in the strong as well as in the weak coupling regime, has several implications.

Firstly, we introduced the concept of *Hermitian Subspace* to identify a subspace (e.g. the one corresponding to a single polariton mode) tailored from a non-Hermitian system and in which Hermiticity is recovered under a specific choice of parameters giving a real dressed eigenenergy. It is worth mentioning that previous findings in PT-symmetric systems (e.g. Ref. [18]) represent a particular case of the more general framework introduced here. In fact, when the system is on resonance, Eq. (5) reduces to the standard PT-symmetry loss balance condition. Consequently, both polariton frequencies become simultaneously real, recovering the characteristic real spectrum of PT-symmetric phases.

Spins and, more specifically, molecular spins, turn out to be an excellent testbed for tuning the different parameters and to span over different regimes when coupled to (planar) microwave resonators. However, our results can be readily transferred and applied also on different paramagnetic spin centers, including defects such as *e.g.* Er^{3+} ions, P donors in Si and Nitrogen-Vacancy centers.

Hermitian subspaces hold potential for the development of fast single-photon switches or modulators for microwave radiation [4]. Fig. 5 displays reflection measurements ($|S_{11}|$) and corresponding theoretical fits, as a function of the externally applied magnetic field B_0 (i.e., at a fixed microwave frequency), corresponding to horizontal line-cuts shown in Fig. 2 (a) and Fig. 4 (b,e). A rather small variation of the magnetic field ($\sim 10^{-4}$ T) is able to switch the reflectivity from its maximum value to nearly

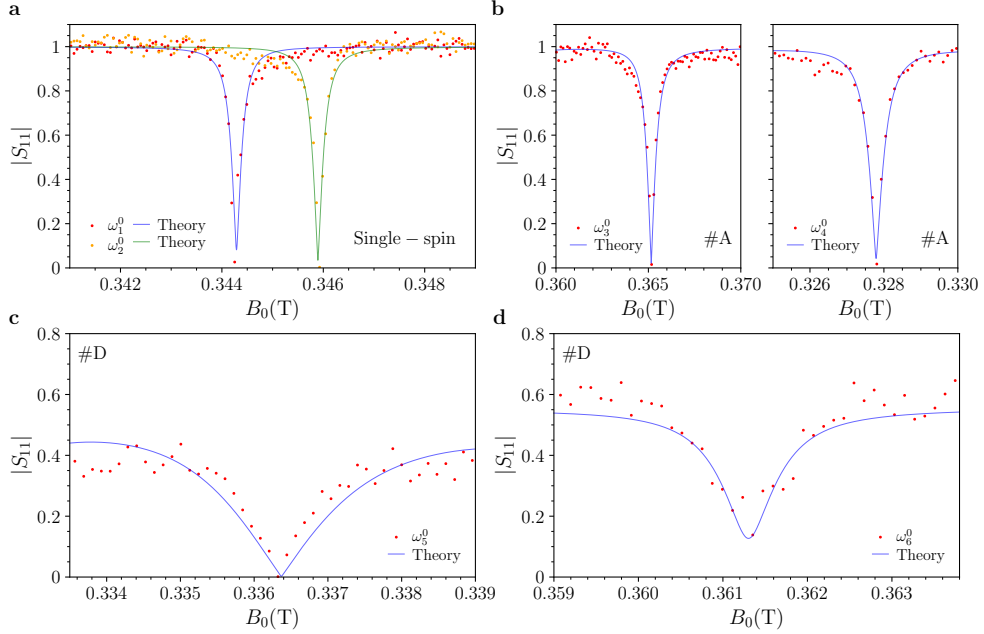


Figure 5 Potential Implementation of Single Microwave Photon Switches. **a** Experimental (red and orange dots) and theoretical (blue and green lines) normalized reflection ($|S_{11}|$) as a function of the static magnetic field B_0 for the BDPA sample (single spin case), highlighting perfect absorption. Data are extracted along the horizontal lines shown in Fig. 2(a) (at fixed frequency, ω_1^0 and ω_2^0). **b** Experimental (red dots) and theoretical (blue lines) normalized reflection $|S_{11}|$ obtained for the VOTPP crystal (position #A) based on the horizontal lines illustrated in Fig. 4(b) (see ω_3^0 and ω_4^0). **c, d** Experimental (red dots) and theoretical (blue lines) normalized reflection $|S_{11}|$ for the VOTPP crystal (position #D), extracted from the horizontal lines shown in Fig. 4(e) (see ω_5^0 and ω_6^0). A small static magnetic field bias (*e.g.* an additional modulation coil) allows a fast tuning of the reflection in and out from the dips, suppressing the microwave photon or allowing its propagation through the antenna.

zero. In this way the reflection can be switched from nearly zero to its maximum or viceversa, suppressing the single microwave photon or allowing it to propagate by simply applying a time-dependent external magnetic field bias (*e.g.* through a modulation coil). We estimate the achievable modulation depth from the data in Fig. 5 as

$$M_d = 20 \log_{10} \left[\frac{|S_{11}^{\text{on}}|}{|S_{11}^{\text{off}}|} \right], \quad (6)$$

where $|S_{11}^{\text{on(off)}}|$ represents the maximum (minimum) value of $|S_{11}|$. Without specific optimization of the experimental setup, we find $M_d \approx 50$ dB for the BDPA by varying B_0 within a range of approximately 4×10^{-4} T (orange dots in Fig. 5 (a)). Notably, this value remains robust against fluctuations in the *on*-state (maximum S_{11}), as the near-zero reflectivity in the *off*-state (minimum S_{11}) dominates the modulation depth. For the VOTPP sample in position #A (Fig. 5 (b)) we observe a shallower dip compared

to BDPA. However, we obtain $M_d \approx 35$ dB using lines $\mu = 3, 4$. This analysis can be extended to the weak coupling regime (Fig. 5 (c,d)), where a minimum $M_d \approx 20$ dB can be reached, even when the *on*-state does not correspond to perfect reflection. The required modulation amplitude can significantly be reduced by reducing the spin decay rates and/or increasing the coupling strength. This potential application as a switch or modulator is not limited to spin ensembles and microwave frequencies, but it can be implemented on very different frequency ranges and in a great variety of systems. Here we notice that using large hyperfine multiplets (8 lines here) would significantly increase the accessible static magnetic field range within a single experiment. We highlight that our proposed implementation is less constrained than PT-symmetric configurations, as light-matter detuning can be adjusted to achieve PA without strictly satisfying the loss condition, thus significantly enlarging the possibility to explore non-Hermitian effects in passive open quantum systems. Finally, we observe that the concept of Hermitian subspaces presented here can also be implemented in non-passive systems, by exploiting detuning to balance gain and losses in the absence of PT-symmetry.

4 Methods

4.1 Derivation of the Reflection Scattering Parameter

To derive the reflection spectrum, we first express the output fields in terms of the input fields using the quantum Langevin equations. This leads to the general relation (see Supplemental Material)

$$\hat{\mathbf{F}}_{\text{out}}(\omega) = \left[-\frac{1}{2}\mathbf{\Gamma} - i(\omega\mathbf{I} - \mathbf{A}) \right] \left[\frac{1}{2}\mathbf{\Gamma} - i(\omega\mathbf{I} - \mathbf{A}) \right]^{-1} \hat{\mathbf{F}}_{\text{in}}(\omega), \quad (7)$$

where $\hat{\mathbf{F}}_{\text{in(out)}}(\omega)$ is the input (output) Langevin force vector. These vectors contain the input (output) operators associated to the different channels, i.e. the antenna (both the radiative and non-radiative components, $\hat{a}_{\text{r,in(out)}}(\omega)$ and $\hat{a}_{\text{nr,in(out)}}(\omega)$, respectively) and the spin ensembles ($\hat{b}_{\mu,\text{in(out)}}(\omega)$).

Since we focus on coherent reflection spectra where the signal enters and is sampled through the radiative port of the antenna, $S_{11}(\omega)$, we assume that $\langle \hat{a}_{\text{nr,in}} \rangle = \langle \hat{b}_{\mu,\text{in}} \rangle = 0$. Therefore, taking the expectation value of Eq. (7), where $\langle \hat{\mathbf{F}}_{\text{in}} \rangle = (\sqrt{\gamma_{\text{r}}} \langle \hat{a}_{\text{r,in}} \rangle, 0, \dots)^T$, and applying the input-output relation for the radiative port, $\hat{a}_{\text{r,out}}(\omega) = \hat{a}_{\text{r,in}}(\omega) - \sqrt{\gamma_{\text{r}}}\hat{a}(\omega)$, we derive the reflection coefficient

$$\begin{aligned} S_{11}(\omega) &= \frac{\langle \hat{a}_{\text{r,out}}(\omega) \rangle}{\langle \hat{a}_{\text{r,in}}(\omega) \rangle} = \frac{-\frac{\gamma_{\text{r}} + \gamma_{\text{nr}}}{2} - i(\omega - \omega_0) + \sum_{\mu=1}^N \frac{g_{\mu}^2}{\frac{\gamma_{\text{sr}\mu}}{2} - i(\omega - \omega_{\text{s}\mu})}}{\frac{\gamma_{\text{r}} + \gamma_{\text{nr}}}{2} - i(\omega - \omega_0) + \sum_{\mu=1}^N \frac{g_{\mu}^2}{\frac{\gamma_{\text{sr}\mu}}{2} - i(\omega - \omega_{\text{s}\mu})}} \\ &= 1 - \frac{\gamma_{\text{r}}}{\frac{\gamma_{\text{r}} + \gamma_{\text{nr}}}{2} - i(\omega - \omega_0) + \sum_{\mu=1}^N \frac{g_{\mu}^2}{\frac{\gamma_{\text{sr}\mu}}{2} - i(\omega - \omega_{\text{s}\mu})}}. \end{aligned} \quad (8)$$

This equation serves as a model for fitting experimental reflectivity spectra. Notably, as pointed out in Sec. 1 and in Ref. [42], the denominator of Eq. (8) corresponds to the characteristic polynomial of the non-Hermitian Hamiltonian $\hat{H}_{\text{NH}}/\hbar = \hat{\alpha}^\dagger(\mathbf{A} - i\mathbf{\Gamma}/2)\hat{\alpha}$, whose zeros are the complex eigenfrequencies Ω_j . The numerator has the same structure as the denominator, differing only in the sign of the damping rate associated with the input-output channel, γ_r . By introducing the effective decay matrix $\tilde{\mathbf{\Gamma}}$, which retains the structure of $\mathbf{\Gamma}$ but with the sign of γ_r reversed, the numerator can be interpreted as the characteristic polynomial of the effective non-Hermitian Hamiltonian $\hat{H}_{\text{eff}}/\hbar = \hat{\alpha}^\dagger(\mathbf{A} - i\tilde{\mathbf{\Gamma}}/2)\hat{\alpha}$, whose eigenfrequencies are $\tilde{\Omega}_j$.

4.2 Derivation of the effective Hamiltonian in the strong coupling regime

In this section we present the derivation for a single spin ensemble of the effective non-Hermitian Hamiltonian in the strong coupling regime. Starting from the quantum Langevin equations for the photon and the collective spin operators presented in the Supplementary Material, we apply the unitary transformation \mathbf{U} defined in Sec. 1 to rotate in the polariton basis, i.e. $\hat{\mathbf{P}} = \mathbf{U}\hat{\alpha}$. Therefore, we obtain the following equations of motion for the polaritonic bosonic operators

$$\partial_t \hat{P}_j = -i\bar{\omega}_j \hat{P}_j - \int_{-\infty}^{\infty} d\omega U_{j1} \sum_{k=r, \text{nr}} \sqrt{\frac{\gamma_k}{2\pi}} \hat{c}_k(\omega) - \int_{-\infty}^{\infty} d\omega U_{j2} \sqrt{\frac{\gamma_s}{2\pi}} \hat{d}(\omega), \quad (9)$$

where \hat{c}_k and \hat{d} are the baths' bosonic operators, which are used to construct the corresponding input (output) operators, $\hat{a}_{k, \text{in(out)}}$ and $\hat{b}_{\text{in(out)}}$ (see Supplementary Materials). $\bar{\omega}_j$ and U_{jk} are the polaritonic eigenfrequencies and Hopfield coefficients, respectively, as defined in the main text.

Following the approach outlined in Refs. [43, 44], we substitute the formal solutions of the equations of motion for $\hat{c}_k(\omega)$ and \hat{d} into Eq. (9). By taking the expectation value of the resulting expression, we obtain

$$\begin{aligned} \partial_t p_j(t) = & -i\bar{\omega}_j p_j(t) - \frac{\gamma_j}{2} p_j(t) - U_{j1} U_{m1}^* \frac{\gamma_r + \gamma_{\text{nr}}}{2} p_m(t) \\ & - U_{j2} U_{m1}^* \frac{\gamma_s}{2} p_m(t) + \sqrt{\gamma_r} U_{j1} a_{\text{in}}(t), \end{aligned} \quad (10)$$

where m is the complementary index of j , i.e. $m = 2$ when $j = 1$ and viceversa. In addition, we introduced the definitions $p_j(t) = \langle \hat{P}_j(t) \rangle$, $\gamma_j = (\gamma_r + \gamma_{\text{nr}}) |U_{j1}|^2 + \gamma_s |U_{j2}|^2$ and $a_{\text{in}}(t) = \langle \hat{a}_{r, \text{in}}(t) \rangle$, which represents the coherent input signal. Specifically, in the derivation of Eq. (10), we took into account that the system has a coherent feeding only through the antenna radiative channel, thus implying $\langle \hat{a}_{\text{nr}, \text{in}} \rangle = \langle \hat{b}_{\text{in}} \rangle = 0$. Eq. (10) can be rewritten in the frequency domain as

$$\begin{aligned} -i\omega p_j(\omega) = & -i\bar{\omega}_j p_j(\omega) - \frac{\gamma_j}{2} p_j(\omega) - U_{j1} U_{m1}^* \frac{\gamma_r + \gamma_{\text{nr}}}{2} p_m(\omega) \\ & - U_{j2} U_{m1}^* \frac{\gamma_s}{2} p_m(\omega) + \sqrt{\gamma_r} U_{j1} a_{\text{in}}(\omega). \end{aligned} \quad (11)$$

By imposing the perfect absorption condition, $a_{out}(\omega) = 0$, we obtain from the input-output relations the explicit expression $a_{in}(\omega) = \sqrt{\gamma_r} (U_{11} p_1(\omega) + U_{12} p_2(\omega))$, which can be inserted in Eq. (11). Furthermore, for $\omega \approx \bar{\omega}_j$, only p_j is significantly excited by the input field, while the terms involving the other polariton mode can be safely neglected in the strong coupling regime, due to the great separation of the spectral lines. Hence, the effective dynamics in the time domain can be written as

$$\partial_t p_j(t) = -i\bar{\omega}_j p_j(t) - \frac{\bar{\gamma}_j}{2} p_j(t), \quad (12)$$

where $\bar{\gamma}_j = (-\gamma_r + \gamma_{nr}) |U_{j1}|^2 + \gamma_s |U_{j2}|^2$, as in Eq. (5). These equations of motions can be derived by the effective non-Hermitian Hamiltonian

$$\hat{H}_{\text{eff}} = \sum_{j=1,2} \left(\bar{\omega}_j - i\frac{\bar{\gamma}_j}{2} \right) \hat{P}_j^\dagger \hat{P}_j, \quad (13)$$

which coincides with Eq. (4). This procedure can be easily generalized in the case of multiple spin resonances, as in the strong coupling regime each photon-spin anti-crossing is separated from the others.

4.3 Experimental Set up

We use a planar superconducting lumped-element LC microwave resonator made of superconducting Niobium films (thickness, 50 nm) on sapphire substrate (thickness, 420 μm) as shown in Fig. 1. The resonator has a small inductive loop to enhance the generated microwave magnetic field, which is coupled to a large interdigitated capacitance. The resonator works in reflection mode, at a fundamental frequency $\omega_0/2\pi \approx 9.9$ GHz, and it is coupled to the input-output line through an antenna, whose position can be adjusted at room temperature, before cooling the sample. The chip carrying the resonator is loaded into a cylindrical copper waveguide sample holder hosting the antenna in his bottom [45, 46]. Preliminary characterization of the empty resonator are reported in Supplementary Information.

All experiments are carried out inside a Qinu Sionludi dilution refrigerator (base temperature 20 mK) equipped with a three-axial superconducting magnet and microwave lines and electronics [45, 46]. The input signal is attenuated by 60 dB inside the cryostat before reaching the sample box with the antenna, while the output line hosts a cryogenic High Electron Mobility Transition (HEMT) amplifier (Low Noise Factory, 37 dB gain). The signal is further amplified at room temperature before acquisition. The complex reflection scattering parameter, S_{11} , is measured with a Vector Network Analyzer (VNA) for different values of the static magnetic field applied, obtaining the 2D maps shown in Fig. 2 and Fig. 4. The input power at the position of the antenna is between -130 and -120 dBm, corresponding to average single microwave photon into the resonator (see Supplementary Information). The cylindrical box and the resonator are aligned into the magnet in order to have the static magnetic field along the plane of the chip, *i.e.* in a in-plane configuration (Fig. 1.c). All the measured

reflection scattering parameters have been normalized over the average value of the signal baseline measured off-resonance.

4.4 Molecular Spin Samples

We use two samples of the molecular compounds shown in Fig. 1 (c). The first one is a diluted solid dispersion of α, γ -bisdiphenylene- β -phenylallyl (BDPA, for short) organic radical into a Polystyrene matrix, with a spin density of $\approx 1 \cdot 10^{15}$ spin/mm³. The sample was prepared as described in [47] and then cut into a rectangular shape with size $\approx 1.5 \times 1$ mm². The sample is placed on the resonator as shown in Fig. 1 (a). Each molecule has electronic spin $S = 1/2$, which is due to its single unpaired electron [47, 48]. Pure BDPA samples typically have antiferromagnetic exchange interaction occurring below 10 K [48–50], with a Curie-Weiss temperature between $T_C = -8$ K and $T_C = -1$ K, strongly dependent by the spin concentration and by the solvent or matrix used [48–50]. Although there are no reports for BDPA diluted in Polystyrene, due to the relatively high concentration, we can expect that a residual antiferromagnetic interaction still occurs among molecules. Therefore, our BDPA sample constitutes a prototypical TLS collection with essentially negligible magnetic anisotropy and no hyperfine splitting, which gives a single transition frequency [47, 48].

The other sample is a single crystal of VOTPP with 2% concentration in its isostructural diamagnetic analog, TiO(TPP). Each molecule has an electronic spin $S = 1/2$ ground state and an additional hyperfine splitting due to the interaction with the $I = 7/2$ nuclear spin of the ⁵¹V ion (natural abundance: 99.75%). This results in a multiplet with eight $\{m_z, I_z\}$ electronuclear transitions, which can be exploited as eight independent spin ensembles. The magnetic properties and the electron spin resonance spectroscopy of this molecule have been previously reported in [20]. In particular, the hyperfine tensor shows uniaxial anisotropy with parallel component $A_{\parallel} = 477$ MHz = 23 mK and perpendicular component $A_{\perp} = 168$ MHz = 8 mK [20], respectively. These relatively-large values, combined with the temperature of the experiments and the frequency of the resonator, give different thermal population on the eight lines, thus decreasing the coupling rate g_{μ} for increasing line number i (see Supplementary Information). The position of the VOTPP crystal (from #A to #D in Fig. 1 (a)) is adjusted before each cooldown. Due to the experimental configuration used and the orientation of the molecules inside the unit cell, all molecules experience the same static magnetic field, which lies on the TPP plane and it is nearly perpendicular to the direction of the $V = 0$ double bound.

Supplementary information. Supplementary Information contains extended theoretical derivations, additional experimental results as well as all fit parameters.

Acknowledgements. We thank Dr. Johan van Tol (National High Magnetic Field Laboratory, Florida, USA) for the preparation of BDPA sample.

We thank Dr. Filippo Troiani (CNR Istituto Nanoscienze, Centro S3, Modena, Italy) for stimulating discussion. C.B. acknowledges the International Excellence Grants Program of KIT for support through the University of Excellence concept.

Declarations

- Funding: This work was funded by the National Quantum Science and Technology Institut (NQSTI) PE00000023 SPOKE 5- call N. 1 Project "Addressing molecular and Spins with MICrowave puLsEs through Superconducting circuits for QUantum Information Processing (SMILE-SQUIP)" and by the US Office of Naval Research award N62909-23-1-2079 project "Molecular Spin Quantum Technologies and Quantum Algorithms". This work was also supported by the International Excellence Grants Program of KIT with funds granted to the University of Excellence concept.
- Conflict of interest/Competing interests: All authors declare no competing interests.
- Ethics approval and consent to participate: n.a.
- Consent for publication: n.a.
- Data availability: Data are available from corresponding author upon reasonable request.
- Materials availability: n.a.
- Code availability: n.a.
- Author contribution: The experiment was conceived and designed by C.B., A.G., M.A. The theoretical framework has been developed by D.L., S.N. and S.S. The measurement were carried out by C.B. and S.G. at Karlsruhe Institute of Technology, under the supervision of W.W.. The resonator were designed by D.R.. Data fitting and simulation were done by D.L. and S.N. (with equal contributions). The VOTPP sample was prepared by F.S., who carried out also the EasySpin simulation of VOTPP. The manuscript was written by C.B. and D.L. with inputs from all coauthors. All authors contributed to the discussion of the results. The manuscript has been revised by all authors before submission.

Editorial Policies for:

Springer journals and proceedings: <https://www.springer.com/gp/editorial-policies>

Nature Portfolio journals: <https://www.nature.com/nature-research/editorial-policies>

Scientific Reports: <https://www.nature.com/srep/journal-policies/editorial-policies>

BMC journals: <https://www.biomedcentral.com/getpublished/editorial-policies>

References

- [1] Bender, C.M., Boettcher, S.: Real spectra in non-hermitian hamiltonians having \mathcal{PT} symmetry. *Phys. Rev. Lett.* **80**, 5243–5246 (1998) <https://doi.org/10.1103/PhysRevLett.80.5243>
- [2] Bender, C.M.: Making sense of non-hermitian hamiltonians. *Reports on Progress in Physics* **70**(6), 947 (2007)
- [3] Özdemir, Ş.K., Rotter, S., Nori, F., Yang, L.: Parity–time symmetry and exceptional points in photonics. *Nature materials* **18**(8), 783–798 (2019)

- [4] Feng, L., El-Ganainy, R., Ge, L.: Non-hermitian photonics based on parity–time symmetry. *Nature Photonics* **11**(12), 752–762 (2017)
- [5] Sun, Y., Tan, W., Li, H.-q., Li, J., Chen, H.: Experimental Demonstration of a Coherent Perfect Absorber with PT Phase Transition. *Phys. Rev. Lett.* **112**, 143903 (2014) <https://doi.org/10.1103/PhysRevLett.112.143903>
- [6] Wenner, J., Yin, Y., Chen, Y., Barends, R., Chiaro, B., Jeffrey, E., Kelly, J., Megrant, A., Mutus, J.Y., Neill, C., O’Malley, P.J.J., Roushan, P., Sank, D., Vainsencher, A., White, T.C., Korotkov, A.N., Cleland, A.N., Martinis, J.M.: Catching time-reversed microwave coherent state photons with 99.4% absorption efficiency. *Phys. Rev. Lett.* **112**, 210501 (2014) <https://doi.org/10.1103/PhysRevLett.112.210501>
- [7] Wang, C., Sweeney, W.R., Stone, A.D., Yang, L.: Coherent perfect absorption at an exceptional point. *Science* **373**(6560), 1261–1265 (2021) <https://doi.org/10.1126/science.abj1028> <https://www.science.org/doi/pdf/10.1126/science.abj1028>
- [8] Baranov, D.G., Krasnok, A., Shegai, T., Alù, A., Chong, Y.: Coherent perfect absorbers: linear control of light with light. *Nature Reviews Materials* **2**(12), 17064 (2017) <https://doi.org/10.1038/natrevmats.2017.64>
- [9] Roger, T., Vezzoli, S., Bolduc, E., Valente, J., Heitz, J.J.F., Jeffers, J., Soci, C., Leach, J., Couteau, C., Zheludev, N.I., Faccio, D.: Coherent perfect absorption in deeply subwavelength films in the single-photon regime. *Nature Communications* **6**(1), 7031 (2015) <https://doi.org/10.1038/ncomms8031>
- [10] Feng, S., Halterman, K.: Coherent perfect absorption in epsilon-near-zero metamaterials. *Phys. Rev. B* **86**, 165103 (2012) <https://doi.org/10.1103/PhysRevB.86.165103>
- [11] Müllers, A., Santra, B., Baals, C., Jiang, J., Benary, J., Labouvie, R., Zezyulin, D.A., Konotop, V.V., Ott, H.: Coherent perfect absorption of nonlinear matter waves. *Science Advances* **4**(8), 6539 (2018) <https://doi.org/10.1126/sciadv.aat6539> <https://www.science.org/doi/pdf/10.1126/sciadv.aat6539>
- [12] Baldacci, L., Zanotto, S., Tredicucci, A.: Coherent perfect absorption in photonic structures. *Rendiconti Lincei* **26**(2), 219–230 (2015) <https://doi.org/10.1007/s12210-015-0428-z>
- [13] Nie, G., Shi, Q., Zhu, Z., Shi, J.: Selective coherent perfect absorption in metamaterials. *Applied Physics Letters* **105**(20), 201909 (2014) <https://doi.org/10.1063/1.4902330> https://pubs.aip.org/aip/apl/article-pdf/doi/10.1063/1.4902330/14305678/201909_1_online.pdf
- [14] Li, S., Luo, J., Anwar, S., Li, S., Lu, W., Hang, Z.H., Lai, Y., Hou, B., Shen, M., Wang, C.: An equivalent realization of coherent perfect absorption under single

- beam illumination. *Scientific Reports* **4**(1), 7369 (2014) <https://doi.org/10.1038/srep07369>
- [15] Li, S., Luo, J., Anwar, S., Li, S., Lu, W., Hang, Z.H., Lai, Y., Hou, B., Shen, M., Wang, C.: Broadband perfect absorption of ultrathin conductive films with coherent illumination: Superabsorption of microwave radiation. *Phys. Rev. B* **91**, 220301 (2015) <https://doi.org/10.1103/PhysRevB.91.220301>
- [16] Chen, L., Kottos, T., Anlage, S.M.: Perfect absorption in complex scattering systems with or without hidden symmetries. *Nature Communications* **11**(1), 5826 (2020) <https://doi.org/10.1038/s41467-020-19645-5>
- [17] Zhang, G.-Q., Wang, Y., Xiong, W.: Detection sensitivity enhancement of magnon Kerr nonlinearity in cavity magnonics induced by coherent perfect absorption. *Phys. Rev. B* **107**, 064417 (2023) <https://doi.org/10.1103/PhysRevB.107.064417>
- [18] Zhang, D., Luo, X.-Q., Wang, Y.-P., Li, T.-F., You, J.Q.: Observation of the exceptional point in cavity magnon-polaritons. *Nature Communications* **8**(1), 1368 (2017)
- [19] Qian, J., Meng, C.H., Rao, J.W., Rao, Z.J., An, Z., Gui, Y., Hu, C.M.: Non-hermitian control between absorption and transparency in perfect zero-reflection magnonics. *Nature Communications* **14**(1), 3437 (2023) <https://doi.org/10.1038/s41467-023-39102-3>
- [20] Yamabayashi, T., Atzori, M., Tesi, L., Cosquer, G., Santanni, F., Boulon, M.-E., Morra, E., Benci, S., Torre, R., Chiesa, M., Sorace, L., Sessoli, R., Yamashita, M.: Scaling up electronic spin qubits into a three-dimensional metal organic framework. *Journal of the American Chemical Society* **140**(38), 12090–12101 (2018) <https://doi.org/10.1021/jacs.8b06733> . tex.eprint: <https://doi.org/10.1021/jacs.8b06733>
- [21] Atzori, M., Tesi, L., Morra, E., Chiesa, M., Sorace, L., Sessoli, R.: Room-temperature quantum coherence and rabi oscillations in vanadyl phthalocyanine: Toward multifunctional molecular spin qubits. *Journal of the American Chemical Society* **138**(7), 2154–2157 (2016) <https://doi.org/10.1021/jacs.5b13408> . tex.eprint: <http://dx.doi.org/10.1021/jacs.5b13408>
- [22] Bader, K., Schlindwein, S.H., Gudat, D., Slageren, J.: Molecular qubits based on potentially nuclear-spin-free nickel ions. *Phys. Chem. Chem. Phys.* **19**(3), 2525–2529 (2017) <https://doi.org/10.1039/C6CP08161D> . Publisher: The Royal Society of Chemistry
- [23] Bader, K., Dengler, D., Lenz, S., Endeward, B., Jiang, S.-D., Neugebauer, P., Van Slageren, J.: Room temperature quantum coherence in a potential molecular qubit. *Nature Communications* **5** 5(5304) (2014)

- [24] Candini, A., Lorusso, G., Troiani, F., Ghirri, A., Carretta, S., Santini, P., Amoretti, G., Muryn, C., Tuna, F., Timco, G., McInnes, E.J.L., Winpenny, R.E.P., Wernsdorfer, W., Affronte, M.: Entanglement in supramolecular spin systems of two weakly coupled antiferromagnetic rings (purple-Cr₇Ni). *Physical Review Letters* **104**(3), 037203 (2010) <https://doi.org/10.1103/PhysRevLett.104.037203> . Number of pages: 4 Publisher: American Physical Society
- [25] Garlatti, E., Guidi, T., Ansbro, S., Santini, P., Amoretti, G., Ollivier, J., Mutka, H., Timco, G., Vitorica-Yrezabal, I.J., Whitehead, G.F.S., Winpenny, R.E.P., Carretta, S.: Portraying entanglement between molecular qubits with four-dimensional inelastic neutron scattering. *Nature Communications* **8**(1), 14543 (2017) <https://doi.org/10.1038/ncomms14543> . tex.refid: Garlatti2017
- [26] Timco, G.A., Carretta, S., Troiani, F., Tuna, F., Pritchard, R.J., Muryn, C.A., McInnes, E.J.L., Ghirri, A., Candini, A., Santini, P., Amoretti, G., Affronte, M., Winpenny, R.E.P.: Engineering the coupling between molecular spin qubits by coordination chemistry. *Nature Nanotechnology* **4**, 173–178 (2009)
- [27] Ghirri, A., Candini, A., Affronte, M.: Molecular spins in the context of quantum technologies. *Magnetochemistry (Basel, Switzerland)* **3**(1), 12 (2017)
- [28] Nakazawa, S., Nishida, S., Ise, T., Yoshino, T., Mori, N., Rahimi, R.D., Sato, K., Morita, Y., Toyota, K., Shiomi, D., Kitagawa, M., Hara, H., Carl, P., Höfer, P., Takui, T.: A synthetic two-spin quantum bit: g-Engineered exchange-coupled biradical designed for controlled-NOT gate operations. *Angewandte Chemie International Edition* **51**(39), 9860–9864 (2012) <https://doi.org/10.1002/anie.201204489> . Publisher: WILEY-VCH Verlag
- [29] Chiesa, A., Macaluso, E., Petiziol, F., Wimberger, S., Santini, P., Carretta, S.: Molecular Nanomagnets as Qubits with Embedded Quantum-Error Correction. *J. Phys. Chem. Lett.* **11**(20), 8610–8615 (2020) <https://doi.org/10.1021/acs.jpcclett.0c02213> . Publisher: American Chemical Society
- [30] Ranieri, D., Santanni, F., Privitera, A., Albino, A., Salvadori, E., Chiesa, M., Totti, F., Sorace, L., Sessoli, R.: An exchange coupled meso–meso linked vanadyl porphyrin dimer for quantum information processing. *Chemical Science* **14**(1), 61–69 (2023) <https://doi.org/10.1039/D2SC04969D> . Publisher: The Royal Society of Chemistry
- [31] Bonizzoni, C., Ghirri, A., Santanni, F., Affronte, M.: Quantum sensing of magnetic fields with molecular spins. *npj Quantum Information* **10**(1), 41 (2024) <https://doi.org/10.1038/s41534-024-00838-5>
- [32] Yu, C.-J., Kugelgen, S., Laorenza, D.W., Freedman, D.E.: A Molecular Approach to Quantum Sensing. *ACS Central Science* **7**(5), 712–723 (2021) <https://doi.org/10.1021/acscentsci.0c00737> . Publisher: American Chemical Society. Accessed 2023-10-19

- [33] Troiani, F., Ghirri, A., Paris, M.G.A., Bonizzoni, C., Affronte, M.: Towards quantum sensing with molecular spins. *Journal of Magnetism and Magnetic Materials* **491**, 165534 (2019) <https://doi.org/10.1016/j.jmmm.2019.165534>
- [34] Bonizzoni, C., Ghirri, A., Affronte, M.: Coherent coupling of molecular spins with microwave photons in planar superconducting resonators. *Advances in Physics: X* **3**(1), 1435305 (2018)
- [35] Bonizzoni, C., Ghirri, A., Atzori, M., Sorace, L., Sessoli, R., Affronte, M.: Coherent coupling between Vanadyl Phthalocyanine spin ensemble and microwave photons: towards integration of molecular spin qubits into quantum circuits. *Scientific Reports* **7**(1), 13096 (2017). tex.refid: Bonizzoni2017
- [36] Bonizzoni, C., Ghirri, A., Santanni, F., Atzori, M., Sorace, L., Sessoli, R., Affronte, M.: Storage and retrieval of microwave pulses with molecular spin ensembles. *npj Quantum Information* **6**(1), 68 (2020). tex.refid: Bonizzoni2020
- [37] Bonizzoni, C., Tincani, M., Santanni, F., Affronte, M.: Machine-Learning-Assisted Manipulation and Readout of Molecular Spin Qubits. *Physical Review Applied* **18**(6), 064074 (2022) <https://doi.org/10.1103/PhysRevApplied.18.064074> . Publisher: American Physical Society. Accessed 2023-10-18
- [38] Ghirri, A., Bonizzoni, C., Troiani, F., Buccheri, N., Beverina, L., Cassinese, A., Affronte, M.: Coherently coupling distinct spin ensembles through a high- T_c superconducting resonator. *Physical Review A: Atomic, Molecular, and Optical Physics* **93**(6), 063855 (2016) <https://doi.org/10.1103/PhysRevA.93.063855> . Number of pages: 7 Publisher: American Physical Society
- [39] Zanotto, S., Tredicucci, A.: Universal lineshapes at the crossover between weak and strong critical coupling in fano-resonant coupled oscillators. *Scientific Reports* **6**(1), 24592 (2016) <https://doi.org/10.1038/srep24592>
- [40] Tadokoro, M., Inoue, T., Tamaki, S., Fujii, K., Isogai, K., Nakazawa, H., Takeda, S., Isobe, K., Koga, N., Ichimura, A., Nakasuji, K.: Mixed-Valence States Stabilized by Proton Transfer in a Hydrogen-Bonded Biimidazolate Rhenium Dimer. *Angewandte Chemie International Edition* **46**(31), 5938–5942 (2007) <https://doi.org/10.1002/anie.200701277> . Publisher: WILEY-VCH Verlag
- [41] Kockum, A.F., Miranowicz, A., Liberato, S.D., Savasta, S., Nori, F.: Ultrastrong coupling between light and matter. *Nature Reviews Physics* **1**(1), 19–40 (2019) <https://doi.org/10.1038/s42254-018-0006-2>
- [42] Lamberto, D., Orlando, G., Savasta, S.: Superradiant Quantum Phase Transition in Open Systems: System-Bath Interaction at the Critical Point (2024). <https://arxiv.org/abs/2411.16514>
- [43] Walls, D.F., Milburn, G.J.: *Quantum information*, pp. 307–346. Springer (2008).

<https://doi.org/10.1007/978-3-540-28574-8>

- [44] Gardiner, C.W., Zoller, P.: Quantum noise: a handbook of Markovian and non-Markovian quantum stochastic methods with applications to quantum optics. Springer (2004)
- [45] Rieger, D., Günzler, S., Spiecker, M., Nambisan, A., Wernsdorfer, W., Pop, I.M.: Fano interference in microwave resonator measurements. *Phys. Rev. Appl.* **20**, 014059 (2023) <https://doi.org/10.1103/PhysRevApplied.20.014059>
- [46] Rieger, D., Günzler, S., Spiecker, M., Paluch, P., Winkel, P., Hahn, L., Hohmann, J.K., Bacher, A., Wernsdorfer, W., Pop, I.M.: Granular aluminium nanojunction fluxonium qubit. *Nature Materials* **22**(2), 194–199 (2023) <https://doi.org/10.1038/s41563-022-01417-9>
- [47] Bonizzoni, C., Maksutoglu, M., Ghirri, A., Tol, J., Rameev, B., Affronte, M.: Coupling sub-nanoliter BDPA organic radical spin ensembles with YBCO inverse anapole resonators. *Applied Magnetic Resonance* **54**(143) (2023) <https://doi.org/10.1007/s00723-022-01505-8> . tex.refid: Bonizzoni2022
- [48] Lenz, S., Kónig, D., Hunger, D., Slageren, J.: Room-temperature quantum memories based on molecular electron spin ensembles. *Advanced Materials* **33**, 2101673 (2021) <https://doi.org/10.1002/adma.202101673>
- [49] Duffy, W., Dubach, J.F., Pianetta, P.A., Deck, J.F., Strandburg, D.L., Miedema, A.R.: Antiferromagnetic linear chains in the crystalline free radical BDPA. *The Journal of Chemical Physics* **56**(6), 2555–2561 (1972) <https://doi.org/10.1063/1.1677580> . tex.eprint: <https://doi.org/10.1063/1.1677580>
- [50] Burgess, J.H., Rhodes, R.S., Mandel, M., Edelstein, A.S.: Magnetic susceptibilities and exchange effects in four organic free radicals. *Journal of Applied Physics* **33**(3), 1352–1353 (1962) <https://doi.org/10.1063/1.1728726> . tex.eprint: <https://doi.org/10.1063/1.1728726>

SUPPLEMENTARY INFORMATION OF:
OBSERVATION OF PERFECT ABSORPTION IN HYPERFINE LEVELS OF MOLECULAR SPINS
WITH HERMITIAN SUBSPACES

Claudio Bonizzoni^{1,2*}, Daniele Lamberto³, Samuel Napoli³, Simon Günzler⁴,
Dennis Rieger⁴, Fabio Santanni⁵, Alberto Ghirri², Wolfgang Wernsdorfer⁴,
Salvatore Savasta³, Marco Affronte^{1,2}

^{1*}Dipartimento di Scienze Fisiche, Informatiche e Matematiche, Università di
Modena e Reggio Emilia, via G. Campi 213/a, Modena, 41125, Italy.

²Istituto Nanoscienze, CNR, via G. Campi 213/a, Modena, 41125, Italy.

³Dipartimento di Scienze matematiche e informatiche, scienze fisiche e scienze della
terra, Università degli Studi di Messina, Via Salita Sperone, c.da Papardo, Messina,
98166, Italy.

⁴Physikalisches Institut, Karlsruhe Institute of Technology, Wolfgang-Gaede-Str. 1,
Karlsruhe, D-76131, Germany.

⁵Dipartimento di Chimica Ugo Schiff, Università degli Studi di Firenze, via della
Lastruccia 3, Sesto Fiorentino (FI), 50019, Italy.

*Corresponding author(s). E-mail(s): claudio.bonizzoni@unimore.it;

Contents

1 Quantum Langevin Equations for the multiple spin ensemble coupled to the electromagnetic resonator	2
2 Additional Experimental Details	4
2.1 Resonators and Cryostat	4
2.2 Estimation of the microwave photon number	5
3 Additional Data	7
3.1 Data for empty resonators	7
3.2 Tuning antenna position on BDPA	8
3.3 Additional Data for VOTPP	9
4 Fit Parameters for all data sets	10
4.1 Parameters for BDPA	10
4.2 Parameters for VOTPP	12

1 Quantum Langevin Equations for the multiple spin ensemble coupled to the electromagnetic resonator

Here, we derive the quantum Langevin equations leading to the reflection scattering parameter in Eq. (3) of the main text. The total Hamiltonian \hat{H}_T for either the VOTPP or the BDPA sample, including their interaction with the electromagnetic resonators and all the reservoir channels, is given by:

$$\hat{H}_T = \hat{H}_S + \hat{H}_B + \hat{H}_I. \quad (\text{S.1})$$

The system Hamiltonian \hat{H}_S is provided in Eq. (1) of the main text. The bare reservoir Hamiltonian is given by

$$\hat{H}_B = \hbar \int_{-\infty}^{+\infty} d\omega \omega \left(\sum_{k=r, \text{nr}} \hat{c}_k^\dagger(\omega) \hat{c}_k(\omega) + \sum_{\mu=1}^N \hat{d}_\mu^\dagger(\omega) \hat{d}_\mu(\omega) \right), \quad (\text{S.2})$$

where \hat{c}_{nr} and \hat{c}_r are the bosonic annihilation operators associated with the internal and radiative losses of the resonator, respectively. Note that \hat{d}_μ represents the annihilation operator describing the reservoir field of the μ -th spin ensemble. Finally, the interaction of the system and the resonator with their corresponding reservoirs is described by (under the rotating wave approximation (RWA) [1, 2])

$$\hat{H}_I = i\hbar \int_{-\infty}^{+\infty} d\omega \left[\sum_{k=r, \text{nr}} \sqrt{\frac{\gamma_k}{2\pi}} (\hat{c}_k(\omega) \hat{a}^\dagger - \hat{c}_k^\dagger(\omega) \hat{a}) + \sum_{\mu=1}^N \sqrt{\frac{\gamma_{s\mu}}{2\pi}} (\hat{d}_\mu(\omega) \hat{b}_\mu^\dagger - \hat{d}_\mu^\dagger(\omega) \hat{b}_\mu) \right], \quad (\text{S.3})$$

where the decay rates are defined in the main text. Following a standard approach to open quantum systems [1, 2], we derive a set of quantum Langevin equations by substituting the solutions of the reservoir operators into the Heisenberg equations of motion for the system operators (the spin ensemble and the resonator):

$$\frac{d}{dt} \hat{\alpha}(t) = -i\mathbf{A}\hat{\alpha}(t) - \frac{1}{2}\mathbf{\Gamma}\hat{\alpha}(t) + \hat{\mathbf{F}}_{\text{in}}(t), \quad (\text{S.4})$$

$$\frac{d}{dt} \hat{\alpha}(t) = -i\mathbf{A}\hat{\alpha}(t) + \frac{1}{2}\mathbf{\Gamma}\hat{\alpha}(t) + \hat{\mathbf{F}}_{\text{out}}(t). \quad (\text{S.5})$$

In the last expressions, we introduced the block matrices

$$\hat{\alpha} = \begin{pmatrix} \hat{a}(t) \\ \hat{b}_1(t) \\ \vdots \\ \hat{b}_N(t) \end{pmatrix}, \quad \mathbf{A} = \begin{pmatrix} \omega_0 & \mathbf{g}^T \\ \mathbf{g} & \omega_s \end{pmatrix}, \quad \mathbf{\Gamma} = \begin{pmatrix} \gamma_r + \gamma_{\text{nr}} & 0 \\ 0 & \gamma_s \end{pmatrix}, \quad (\text{S.6})$$

where $\boldsymbol{\omega}_s$ and $\boldsymbol{\gamma}_s$ are diagonal block matrices with the μ -th elements given by $\omega_{s\mu}$ and $\gamma_{s\mu}$ (where μ ranges from 1 to N), respectively. Additionally, we defined

$$\mathbf{g}^T = (g_1, \dots, g_N), \quad (\text{S.7})$$

and the input and output field vectors as

$$\hat{\mathbf{F}}_{\text{in}}(t) = \begin{pmatrix} \sqrt{\gamma_r} \hat{a}_{r,\text{in}}(t) + \sqrt{\gamma_{\text{nr}}} \hat{a}_{\text{nr},\text{in}}(t) \\ \sqrt{\gamma_{s1}} \hat{b}_{1,\text{in}}(t) \\ \vdots \\ \sqrt{\gamma_{sN}} \hat{b}_{N,\text{in}}(t) \end{pmatrix}, \quad \hat{\mathbf{F}}_{\text{out}}(t) = \begin{pmatrix} \sqrt{\gamma_r} \hat{a}_{r,\text{out}}(t) + \sqrt{\gamma_{\text{nr}}} \hat{a}_{\text{nr},\text{out}}(t) \\ \sqrt{\gamma_{s1}} \hat{b}_{1,\text{out}}(t) \\ \vdots \\ \sqrt{\gamma_{sN}} \hat{b}_{N,\text{out}}(t) \end{pmatrix}. \quad (\text{S.8})$$

where the components of the input vector are given by

$$\begin{aligned} \hat{a}_{r,\text{in}}(t) &= \frac{1}{\sqrt{2\pi}} \int_{-\infty}^{+\infty} d\omega e^{-i\omega(t-t_0)} \hat{c}_r(\omega; t_0), \\ \hat{a}_{\text{nr},\text{in}}(t) &= \frac{1}{\sqrt{2\pi}} \int_{-\infty}^{+\infty} d\omega e^{-i\omega(t-t_0)} \hat{c}_{\text{nr}}(\omega; t_0), \\ \hat{b}_{\mu,\text{in}}(t) &= \frac{1}{\sqrt{2\pi}} \int_{-\infty}^{+\infty} d\omega e^{-i\omega(t-t_0)} \hat{d}_{\mu}(\omega; t_0). \end{aligned} \quad (\text{S.9})$$

where $t_0 < t$ is the initial time (input) chosen to solve the equations of motion for the reservoir field operators. Similarly, the output field vector entries have the same form as in Eq. (S.9), except that t_0 is replaced by t_f ($t < t_f$, output). Rewriting the Langevin equations Eq. (S.4) and Eq. (S.5) in the frequency domain allows us to express $\mathbf{F}_{\text{out}}(\omega)$ in terms of $\mathbf{F}_{\text{in}}(\omega)$:

$$\hat{\mathbf{F}}_{\text{out}}(\omega) = \left[-\frac{1}{2}\boldsymbol{\Gamma} - i(\omega\mathbf{I} - \mathbf{A}) \right] \left[\frac{1}{2}\boldsymbol{\Gamma} - i(\omega\mathbf{I} - \mathbf{A}) \right]^{-1} \hat{\mathbf{F}}_{\text{in}}(\omega), \quad (\text{S.10})$$

where \mathbf{I} is the identity matrix. Moreover, the input-output relationships are derived by subtracting Eq. (S.4) to Eq. (S.5) in the frequency domain, namely

$$\hat{\mathbf{F}}_{\text{out}}(\omega) = -\boldsymbol{\Gamma} \hat{\boldsymbol{\alpha}}(\omega) + \hat{\mathbf{F}}_{\text{in}}(\omega). \quad (\text{S.11})$$

From this equation follows the input-output relation for the radiative port, $\hat{a}_{r,\text{out}}(\omega) = \hat{a}_{r,\text{in}}(\omega) - \sqrt{\gamma_r} \hat{a}(\omega)$, which is used to calculate the complex scattering coefficient (see Methods).

2 Additional Experimental Details

2.1 Resonators and Cryostat

Each chip used in the experiments is made of sapphire with dimensions $3 \times 10 \text{ mm}^2$ and thickness $420 \mu\text{m}$. The short side of the chip carries two planar microwave resonators, namely Res #1 and Res #2, working in reflection mode and coupled to the same feeding antenna, whose position can be adjusted at room temperature, as in Fig. S1 and Fig. (1) of main text. The two resonators are made of superconducting Niobium films (thickness, 50 nm). The geometry is a lumped-element LC resonator, in which the interdigitated part acts as a large capacitance and the central loops give a small inductance, giving large microwave currents around the loop position. The width of the superconducting niobium strip is $w = 10 \mu\text{m}$, while the interspace between each part of the capacitors is $w' = 20 \mu\text{m}$. The length of the resonator is $l_1 = 1 \text{ mm}$, while its distance from the edge of the chip is $d_1 = 190 \mu\text{m}$. Res #1 and Res #2 are designed to have two fundamental resonant frequency $\omega_{0,1}/2\pi = \nu_{0,1} \approx 9.9 \text{ GHz}$ and $\omega_{0,2}/2\pi = \nu_{0,2} \approx 11 \text{ GHz}$, respectively. The large detuning between their bare resonance frequencies makes Res #1 and #2 fully independent each other. In this work only data obtained from Res #1 are presented.

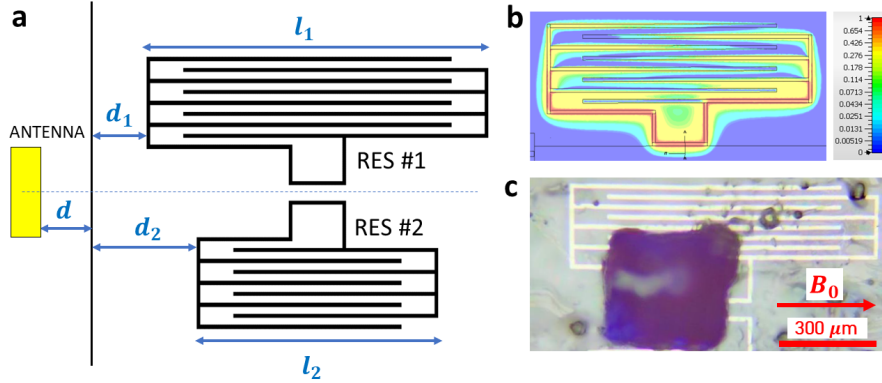


Figure S1: **a** Sketch of the two resonators and of their position with respect to the input-output antenna. **b** Electromagnetic simulation of the bare resonator showing the distribution of the magnitude of the magnetic component of the microwave field. The colorscale on right is normalized on the maximum field value, with red corresponding to maximum and blue to 0. **c** Photo of the planar niobium lumped element resonator with a VOTPP crystalline sample on it. The sample has been partially moved to show the underlying inductive loop of the resonator. Red arrow shows the direction of the applied static magnetic field, B_0 .

The chip is loaded into the same sample holder described in Refs. [3–5], which is essentially a cylindrical copper waveguide hosting the antenna in its bottom part. The

sample holder is cooled inside a Qiniu Sionludi dilution refrigerator with a base temperature of 20 mK, and equipped with three-axial superconducting coils and microwave lines and electronics [3, 4]. The chip and the sample holder are oriented the way that the main coil generates the static magnetic field in the plane of the resonators.

2.2 Estimation of the microwave photon number

We estimate the average number of microwave photons, n_{av} , in the resonator as reported in [6], using Eq. (S.12):

$$n_{av} = \frac{P_{in} Q_{L,1} 10^{-\frac{IL_1}{20}}}{\pi h \nu_{0,1}^2}. \quad (\text{S.12})$$

Here, P_{in} is the input power at the input-output antenna, $Q_{L,1}$ is the loaded quality factor, IL_1 is the insertion loss of the resonator Res. #1 and $\nu_{0,1}$ its resonant frequency. h is Planck's constant. The calculation as a function of the input power is shown in Fig. S2. The input power values used in this work give an average unitary photon number into the resonator.

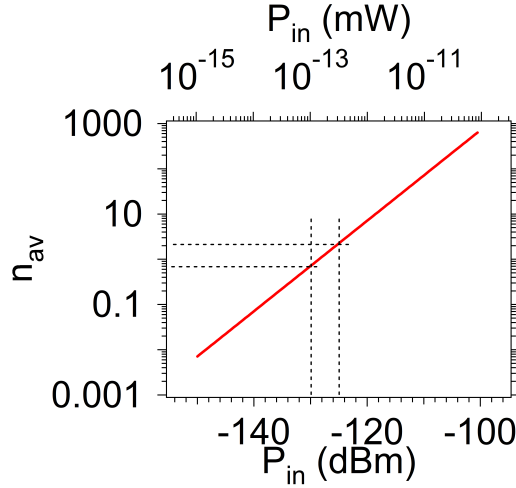


Figure S2: Average number of microwave photons in Res. #1 calculated with Eq. (S.12) as a function of the input power at the antenna. Vertical dashed lines show the range of power values used in this work, corresponding to a single photon on average filling the resonator.

Due to the low photon number used, the temperature and the resonant frequency we estimate the contribution of thermal photons to the photon number. To this end, we consider the resonator as a black body at a given finite temperature, T , and we consider Planck's law:

$$P_{th} = \frac{8\pi h\nu^3}{c^3} \frac{1}{e^{\frac{h\nu}{\kappa_B T}} - 1}. \quad (\text{S.13})$$

Eq. (S.13) gives the power emitted per unit of frequency, ν , unit of solid angle and unit of surface. Here, h is again Planck's constant, while κ_B is Boltzmann's constant and c is the speed of light in vacuum. The number of thermal photons per unit of time, frequency, solid angle and surface, n_{th} (which corresponds to the number of photons per unit of solid angle and surface), is obtained by dividing Eq. (S.13) by the energy of a single photon, $h\nu$. This brings to:

$$n_{th} = \frac{P_{th}}{h\nu} = \frac{8\pi\nu^2}{c^3} \frac{1}{e^{\frac{h\nu}{\kappa_B T}} - 1}. \quad (\text{S.14})$$

Fig. S3 shows the results obtained with Eq. (S.14) as a function of frequency for different experimental temperature values. The results show that at the resonant frequency of Res. #1 (≈ 9.9 GHz, vertical dashed line) the power associated to thermal photon emission is much lower than the input microwave one. Moreover, the corresponding number of photons per unit of solid angle and surface is negligible with respect to the average microwave photon number of the microwave tone. Therefore, the effect of thermal photons can be neglected in our measurements.

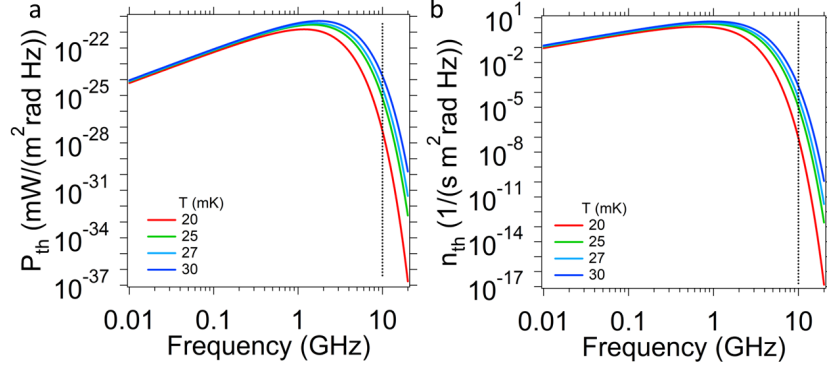


Figure S3: **a** Power per unit of frequency, solid angle and surface as a function of frequency calculated with Eq. (S.13) for different experimental temperatures values used. **b** Number of photons per unit of solid angle and surface calculated with Eq. (S.14) as a function of frequency. In both a and b vertical dashed lines indicated the frequency of Res. #1.

3 Additional Data

3.1 Data for empty resonators

An example of complex reflection scattering parameter (amplitude, $|S_{11}|$, and phase) measured at 30 mK on Resonator Res #1, at microwave power equivalent to single photon level and in zero magnetic field is shown in Fig. S4. Black line is a fit performed by means of Eq. (3) of main paper keeping $g_\mu = 0$ for any μ .

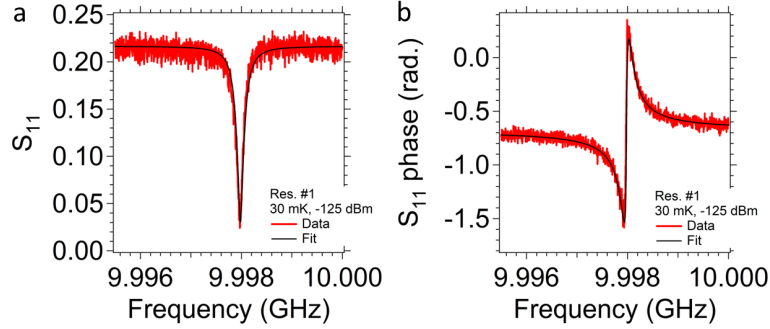


Figure S4: Reflection and phase signals measured at 30 mK and single photon powers for a resonator as the one shown in Fig. 1 of main text. Dashed line are fits based on Eq. (3) of main paper with fixed $g_\mu = 0$ for any μ .

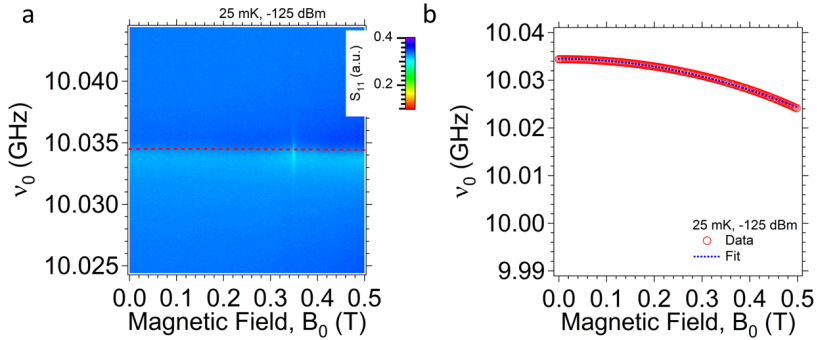


Figure S5: 2D reflection map **a** and resonant frequency as a function of the static in-plane magnetic field **b** for resonator Res. #1. Dashed line is a fit based on Eq. (S.15).

Fig. S5 shows the reflection map for the empty resonator Res. #1 taken at 25 mK for different applied in-plane magnetic field values. The resonance can be measured at least up to $B_0 = 0.5$ T. No signal, except for a very weak one due to magnetic

impurities, and no dips with zero reflection are visible in the range in which the resonance with spins is expected (≈ 0.34 T). The resonant frequency decreases as a function of the static magnetic field as expected from the magnetic field response of niobium under applied in-plane field. While this change in frequency is almost negligible for the single-ensemble results it becomes more heavier on the multiple ensemble data due to the larger field span used. We take into account this effect by including in our model the dependence of the resonant frequency on the static magnetic field correction of the resonant frequency of the resonator according to:

$$\omega_0(B_0)/2\pi = \nu_0(B_0) = \bar{\nu}_0 - aB_0^2. \quad (\text{S.15})$$

Here, $\bar{\nu}_0$ is the bare resonator frequency at zero field and a a phenomenological parameter. The value of a is obtained by fitting the in-plane dependence of the frequency of the resonator for an empty resonator (Fig. S5).

3.2 Tuning antenna position on BDPA

Figure S6 shows 2D normalized reflection maps measured for the BDPA sample for different positions of the input-output antenna. The BDPA sample is placed in similar positions over different experiments to obtain strong coupling regimes similar to the one of Fig. 2 of main paper. The position of the antenna is changed at room temperature before cooldown. We investigate the effect of four different positions, named as Ant. #1 to Ant. #4 in Fig. S6, and corresponding to different decreasing coupling strengths between the antenna and the resonator. An avoided crossing is always visible in the 2D map around resonance, as in Fig. 2 of the main paper. The changes in the bare resonator frequency can be attributed to the different cooldown cycles and to the different coupling with the input-output antenna. Specifically, in Fig. S6 (a, d), $|S_{11}|$ approaches zero for each polariton, indicating the occurrence of perfect absorption away from the central resonance. This is confirmed by the occurrence of two zeroes in the corresponding imaginary part of the eigenfrequencies, $\tilde{\Omega}_j$ (Fig. S6 (c, f)). In contrast, antenna positions Ant. #3 and Ant. #4 (Fig. S6 (g, l)) exhibit an anticrossing with higher reflection values and no signature of perfect absorption. The corresponding fit results confirm a significant reduction in γ_r relative to Fig. S6 (a, d) (see tables in Sec. 4). This reduction influences the imaginary parts of the eigenfrequencies $\tilde{\Omega}_j$, giving no zeroes around resonance.

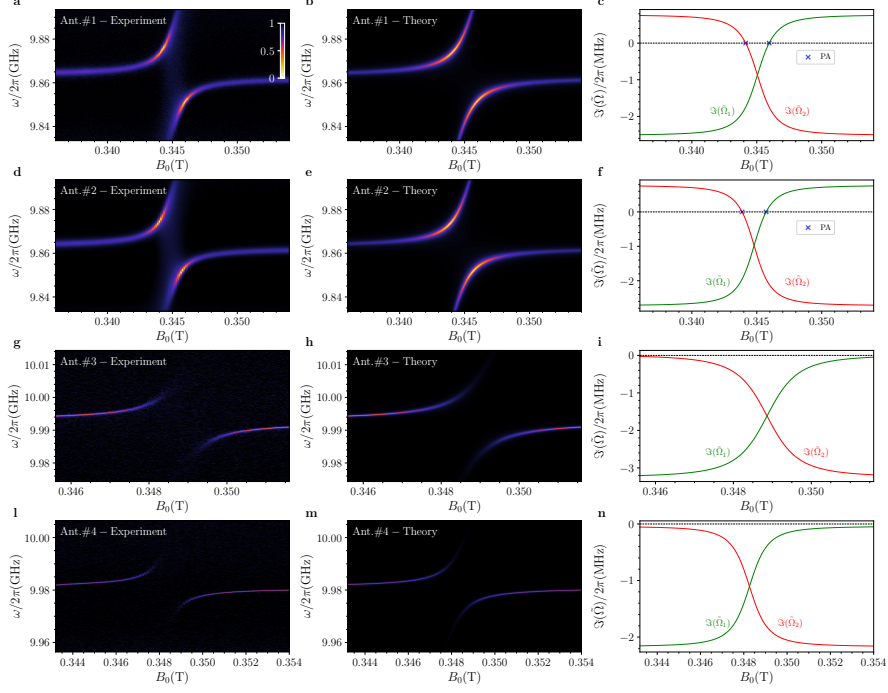


Figure S6: **a, d, g, l** Normalized reflection maps ($|S_{11}|$) measured on BDPA for various positions of the input-output antenna, labeled Ant. #1 to Ant. #4. These correspond to decreasing coupling strengths between the antenna and the resonator (i.e., decreasing γ_r). Note that the map for Ant. #1 is identical to the one shown in Fig. 2 (a) of main text. **b, e, h, m** Reflection maps obtained by fitting the data in **a, d, g, l** using Eq. 8 in Methods. **c, f, i, n** Imaginary parts of the eigenfrequencies $\tilde{\Omega}_j$, extracted from the fitted parameters, confirm the presence of perfect absorption in the cases shown in **a, d**, and its absence in **g, i**.

3.3 Additional Data for VOTPP

Fig. S7 shows the extended data set for the VOTPP crystal. By changing the position of the crystal on the resonator (see Fig. 1 of main text) it is possible to tune the coupling between spins and resonator and to investigate different coupling regimes. Position #A (Fig. S7 (a,b,c)) and #D (Fig. S7 (l,m,n)) correspond to the results reported in main text, while positions #B and #C show intermediate sample positions. The overall coupling regime is mainly determined by the sample position, while a finer tuning is achieved through the different thermal populations of the lines. Our model perfectly fits all experimental data. The real, $\Re(\tilde{\Omega}_j)$, and imaginary, $\Im(\tilde{\Omega}_j)$, part of the polaritonic eigenstates correctly predict the positions and number of dips for all experimental dataset.

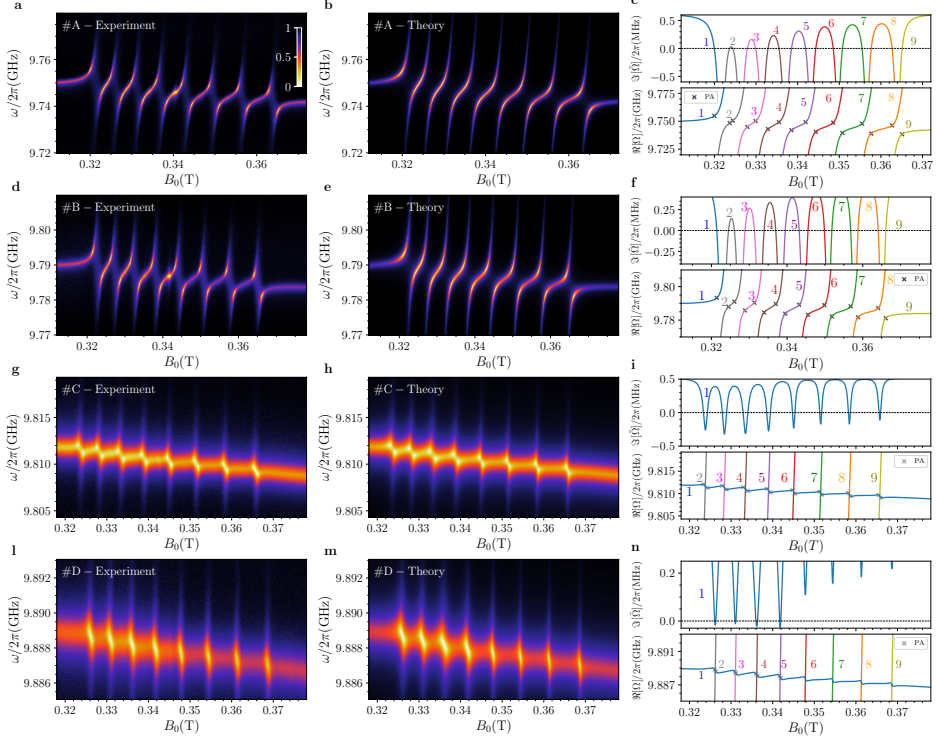


Figure S7: Extended dataset showing the results for all four positions of the VOTPP sample on the resonator (from #A to #D, see Fig. (1) of main text). For each position the measured 2D reflection map, the corresponding fit obtained with Eq. (3) of the main paper are shown. The third column show the Imaginary, $\Im(\tilde{\Omega}_j)$, and Real, $\Re(\tilde{\Omega}_j)$, part of the polaritonic frequencies. All dips are correctly predicted at the energies giving zero imaginary part.

4 Fit Parameters for all data sets

The following tables summarize the fit parameters extracted by means of Eq. (3) of main paper for all experimental datasets shown in the main text and in Sec. 3.3. Each table gives the parameters of the resonator obtained far from resonance and, then, the fit parameters for each μ^{th} spin ensemble.

4.1 Parameters for BDPA

Table S1, Table S2, Table S3 and Table S4 shows the fit parameters for the experimental dataset of BDPA given in Sec. 3.2. The parameters in Table S1 are the ones corresponding also to the data shown in Fig. (2) of main text. The coupling strength is larger than the corresponding linewidth further supporting that BDPA is in the strong coupling regime.

Table S1: $S_{11}(\omega)$ fitting parameters for the BDPA dataset shown in Fig. 2 of main text and in Fig. S6 (Ant. #1).

Resonator parameters			
α (MHz/T ²)	ν_0 (GHz)	$\gamma_r/2\pi$ (MHz)	$\gamma_{nr}/2\pi$ (MHz)
0	9.863	1.67	0.13

Spin ensemble parameters		Coupling strength
g_L	$\gamma_s/2\pi$ (MHz)	$g/2\pi$ (MHz)
2.042	5.04	20.67

Table S2: $S_{11}(\omega)$ fitting parameters for the BDPA dataset shown in Fig. S6 (Ant. #2).

Resonator parameters			
α (MHz/T ²)	ν_0 (GHz)	$\gamma_r/2\pi$ (MHz)	$\gamma_{nr}/2\pi$ (MHz)
0	9.863	1.64	0.094

Spin ensemble parameters		Coupling strength
g_L	$\gamma_s/2\pi$ (MHz)	$g/2\pi$ (MHz)
2.044	5.46	19.73

Table S3: $S_{11}(\omega)$ fitting parameters for the BDPA dataset shown in Fig. S6 (Ant. #3).

Resonator parameters			
α (MHz/T ²)	ν_0 (GHz)	$\gamma_r/2\pi$ (MHz)	$\gamma_{nr}/2\pi$ (MHz)
0	9.993	0.16	0.056

Spin ensemble parameters		Coupling strength
g_L	$\gamma_s/2\pi$ (MHz)	$g/2\pi$ (MHz)
2.047	6.51	12.02

Table S4: $S_{11}(\omega)$ fitting parameters for the BDPA dataset shown in Fig. S6 (Ant. #4).

Resonator parameters			
α (MHz/T ²)	ν_0 (GHz)	$\gamma_r/2\pi$ (MHz)	$\gamma_{nr}/2\pi$ (MHz)
0	9.981	0.06	0.132

Spin ensemble parameters		Coupling strength
g_L	$\gamma_s/2\pi$ (MHz)	$g/2\pi$ (MHz)
2.048	4.34	12.78

4.2 Parameters for VOTPP

Table S5, Table S6, Table S7, Table S8 show the fit parameters extracted from positions #A, #B, #C and #D, respectively (Fig. 4 of main text and Fig. S7). Overall, the coupling strength g_μ of each table decrease from position #A to #D, as a result of the lower amplitude of the microwave field of the resonator felt by the spins. Interestingly, for each sample position dataset, the fitted coupling strength decrease with increasing ensemble (line) index μ , as a result of the different thermal population of each line, as discussed in main text. For position #A all fitted coupling strengths, g_μ , are comparable to their corresponding linewidths, suggesting that the high cooperativity spin-photon coupling regime is achieved. A similar condition is observed also for position #B. Conversely, for position #C and #D each linewidth is significantly larger than its corresponding coupling strength, further suggesting that the weak spin-photon coupling regime is achieved. We attribute this overall increase of the spins decay-rates to the Purcell effect [7, 8]. Specifically, increasing such overlap converts a fraction of the spins decay-rates (spontaneous emission) into an increase of the emission in the resonator mode, which is described by the resonator-spins coupling rates.

Table S5: $S_{11}(\omega)$ fitting parameters for VOTPP in position #A, corresponding to the dataset shown in Fig. 4 of main text and in Fig. S7 (a,b,c).

Resonator parameters			
α (MHz/T ²)	ν_0 (GHz)	$\gamma_r/2\pi$ (MHz)	$\gamma_{nr}/2\pi$ (MHz)
66.62	9.754	1.37	0.12

Spin ensemble parameters			Coupling strengths
μ	$g_{L,\mu}$	$\gamma_{s\mu}/2\pi$ (MHz)	$g_\mu/2\pi$ (MHz)
1	2.166	13.17	15.92
2	2.135	10.25	15.51
3	2.101	9.28	15.14
4	2.066	10.67	14.70
5	2.029	8.35	14.06
6	1.991	7.74	13.54
7	1.952	8.23	12.99
8	1.913	10.39	12.43

Table S6: $S_{11}(\omega)$ fitting parameters for VOTPP in position #B, corresponding to the dataset shown in Fig. S7 (d,e,f).

Resonator parameters			
α (MHz/T ²)	$\bar{\nu}_0$ (GHz)	$\gamma_r/2\pi$ (MHz)	$\gamma_{nr}/2\pi$ (MHz)
70.93	9.795	1.46	0.15

Spin ensemble parameters			Coupling strengths
μ	$g_{L,\mu}$	$\gamma_{s\mu}/2\pi$ (MHz)	$g_\mu/2\pi$ (MHz)
1	2.166	17.40	12.71
2	2.135	13.16	12.33
3	2.102	12.49	12.02
4	2.067	13.12	11.59
5	2.030	12.57	11.12
6	1.993	10.29	10.64
7	1.954	10.60	10.21
8	1.915	12.39	9.81

Table S7: $S_{11}(\omega)$ fitting parameters for VOTPP in position #C, corresponding to the dataset shown in Fig. S7 (g,h,i).

Resonator parameters			
α (MHz/T ²)	$\bar{\nu}_0$ (GHz)	$\gamma_r/2\pi$ (MHz)	$\gamma_{nr}/2\pi$ (MHz)
65.81	9.818	1.59	0.56

Spin ensemble parameters			Coupling strengths
μ	$g_{L,\mu}$	$\gamma_{s\mu}/2\pi$ (MHz)	$g_\mu/2\pi$ (MHz)
1	2.165	40.91	3.91
2	2.135	37.97	3.88
3	2.102	43.82	4.17
4	2.068	35.45	3.67
5	2.031	26.26	3.08
6	1.994	24.01	2.83
7	1.955	23.66	2.82
8	1.916	23.80	2.72

Table S8: $S_{11}(\omega)$ fitting parameters for VOTPP in position #D, corresponding to the dataset shown in Fig. 4 of main paper and in Fig. S7 (l,m,n).

Resonator parameters			
α (MHz/T ²)	ν_0 (GHz)	$\gamma_r/2\pi$ (MHz)	$\gamma_{nr}/2\pi$ (MHz)
47.76	9.894	1.58	0.45

Spin ensemble parameters			Coupling strengths
μ	$g_{L,\mu}$	$\gamma_{s\mu}/2\pi$ (MHz)	$g_{\mu}/2\pi$ (MHz)
1	2.166	49.18	3.72
2	2.134	45.88	3.52
3	2.102	56.31	3.98
4	2.067	39.12	3.33
5	2.031	28.14	2.50
6	1.993	23.51	2.18
7	1.955	21.23	2.02
8	1.916	21.35	1.94

References

- [1] Walls, D.F., Milburn, G.J.: Quantum information, pp. 307–346. Springer (2008). <https://doi.org/10.1007/978-3-540-28574-8>
- [2] Gardiner, C.W., Zoller, P.: Quantum noise: a handbook of Markovian and non-Markovian quantum stochastic methods with applications to quantum optics. Springer (2004)
- [3] Rieger, D., Günzler, S., Spiecker, M., Nambisan, A., Wernsdorfer, W., Pop, I.M.: Fano interference in microwave resonator measurements. *Phys. Rev. Appl.* **20**, 014059 (2023) <https://doi.org/10.1103/PhysRevApplied.20.014059>
- [4] Rieger, D., Günzler, S., Spiecker, M., Paluch, P., Winkel, P., Hahn, L., Hohmann, J.K., Bacher, A., Wernsdorfer, W., Pop, I.M.: Granular aluminium nanojunction fluxonium qubit. *Nature Materials* **22**(2), 194–199 (2023) <https://doi.org/10.1038/s41563-022-01417-9>
- [5] Borisov, K., Rieger, D., Winkel, P., Henriques, F., Valenti, F., Ionita, A., Wessbecher, M., Spiecker, M., Gusenkova, D., Pop, I.M., Wernsdorfer, W.: Superconducting granular aluminum resonators resilient to magnetic fields up to 1 Tesla. *Applied Physics Letters* **117**(12), 120502 (2020) <https://doi.org/10.1063/5.0018012> https://pubs.aip.org/aip/apl/article-pdf/doi/10.1063/5.0018012/14537442/120502.1_online.pdf
- [6] Sage, J.M., Bolkhovsky, V., Oliver, W.D., Turek, B., Welander, P.B.: Study of loss in superconducting coplanar waveguide resonators. *Journal of Applied Physics* **109**(6), 063915 (2011) <https://doi.org/10.1063/1.3552890> . Number: 063915
- [7] Zhang, D., Luo, X.-Q., Wang, Y.-P., Li, T.-F., You, J.Q.: Observation of the exceptional point in cavity magnon-polaritons. *Nature Communications* **8**(1), 1368 (2017)
- [8] Zhang, X., Zou, C.-L., Jiang, L., Tang, H.X.: Strongly coupled magnons and cavity microwave photons. *Phys. Rev. Lett.* **113**, 156401 (2014) <https://doi.org/10.1103/PhysRevLett.113.156401>